HU ISSN 2063-6792

MATERIALS SCIENCE AND ENGINEERING

A Publication of the University of Miskolc

Volume 39, Number 1 (2014)

Miskolc University Press
2014

HU ISSN 2063-6792

CONTENTS

Materials Science and Engineering, Volume 39, No. 1 (2014), pp. 5–13.

DETERMINATION OF THE ANTIMONY- AND STRONTIUM-CONTENT OF ALUMINIUM ALLOYS BY INDUCTIVELY COUPLED PLASMA ATOM EMISSION SPECTROMETRY (ICP-AES) USING A WET CHEMICAL SAMPLE PREPARATION PROCEDURE

OLIVÉR BÁNHIDI[1]

Strontium and especially antimony are not commonly occurring alloying elements in aluminium alloys, therefore their determination by conventional emission spectrometric (OES or XRF) methods might suffer from some difficulties as the certified reference materials needed for the calibration of the spectrometric measurements are not at the disposal of the analysts in many cases. In such cases the instrumental methods, which use wet chemical sample preparation methods by dissolving the sample, may prove rather useful and are frequently applied. In this paper an analytical method developed for the determination of the above-mentioned elements in aluminium alloys is presented. The different steps of the chemical sample preparation procedure and the spectrochemical parameters of the analysis have been selected after careful study.

Keywords: determination of antimony and strontium, aluminium alloy wet chemical sample preparation, spectral interferences.

Introduction

Metals and alloys are frequently analysed by methods using solid samples. These are fast and provide reliable results. Because of the traceability the calibration must be carried out with special care and the interference effects of the sample matrix components have to be eliminated by different correction procedures. Both for calibration and for corrections certified reference materials (CRMs) must be applied, however there are many cases when the suitable CRMs are not at the disposal of the laboratory. Frequently this is the case when a new type of alloy or a new alloying or micro-alloying element is applied and its concentration in the sample has to be determined. Applying an instrumental method, which needs to transform the sample into liquid phase can be a solution for the problem. With a suitable method any kind of solid sample can be taken into solution. In case of liquid samples the calibration and correction of matrix effects can be carried out more easily, as several multielement solutions are available, so neither calibration nor correction means any problem in liquid phase. Strontium and especially antimony are regarded as common alloying or micro-alloying elements in aluminium alloys, therefore it is rather complicated to get high quality CRMs needed both for calibration and for

---

[1] University of Miskolc, Institute of Chemistry
3515 Miskolc-Egyetemváros, Hungary
akmbo@uni-miskolc.hu

matrix-effect correction. By choosing an instrumental method using liquid-phase samples both processes can be carried out with CRM solutions that are easiy to obtain.

So that the present results could be compared to those measured earlier, we used the same procedure to evaluate the signals and to present the effects we experienced.

1. Experimental

1.1. The analytical method

In search for an adequate instrumental method flame or graphite-furnace atomic absorption (FAAS/GFAAS) or ICP-AES can be taken into account. FAAS is cheap and fast – in case of two elements per sample, - but its detection power is insufficient for both elements. The detection ability of GFAAS is excellent for both elements, but it is much slower and suffers from a lot of chemical interferences, so the development of a suitable method would need much time and effort to be carried out. ICP-AES also has sufficient detection power for these components, it is a multielement method therefore it is fast, and besides that it is featured with much less number chemical interference effects than GFAAS even in case of an axially viewed ICP spectrometer.

Considering the above-mentioned features ICP-EAS has been chosen as an eligible method for the measurements. The determinations were carried out with a Varian-make ICP spectrometer, its type is 720 ES.

1.2. The sample preparation procedure

Wet chemical sample preparation means that the sample has to be taken into solution either by simple dissolution or by fusion followed by dissolution. As most of the chemical agents applied in the course of the preparation procedure remain in the solution to be measured, these procedures suffer from two main drawbacks. On one hand the impurities of the reagents must be taken care of, on the other hand the total salt concentration should not be very high as it would substantially reduce the nebulisation efficiency. When choosing the preparation method, both effects must be taken into account.

Aluminium alloys can be dissolved in several ways, thus, the chemical composition of the alloy will determine which method proves suitable.

Unalloyed aluminium, ALMg and AlZn alloys with low silicon content can be dissolved in hydrochloric acid. AlCu alloys must be treated with hydrochloric acid first, then nitric acid is to be added when the initial intense reaction has subsided [1].

Alloys with higher silicon content will dissolve neither in hydrochloric acid nor in the mixture of hydrochloric and nitric acid. In such cases, two possibilities remain. One of them is to dissolve the sample in a mixture of hydrofluoric acid and nitric acid in a closed PTFE bomb, the other is to take the sample into solution in sodium hydroxide and then to acidify the solution with the addition of nitric and hydrochloric acid [2]. Aluminium and silicon can be dissolved in the alkaline media, while the acids will take into solution the components insoluble in NaOH.

This later method is featured by a high salt content, therefore it can be applied only in case of limited sample mass (approximately 0.1 g) so that the extremely high salt concentration of the solution could be avoided.

The type of the analysed alloy was AlSi9Cu2,5, its chemical composition can be seen in Table 1.

Table 1

Concentration of the main components of the alloy to be analysed
(each data in the Table is given in m/m %)

Si	Cu	Mg	Zn	Fe	Mn	Ni	Ti
9.32	2.51	0.31	0.61	0.51	0.37	0.037	0.097

Considering the high silicon content it could not be expected that the sample would dissolve in hydrochloric acid, therefore the application of the PTFE bomb method with nitric acid and hydrofluoric acid was determined. Though this method has been used for the dissolution of several aluminium alloys having medium or high silicon content, unfortunately this mixture of acids failed to dissolve the respective type of alloy. Consequently the alkaline method had to be chosen. So as to keep the salt concentration of the solutions to be analysed relatively low, the sample mass used for the preparation was around 0.1 g and the sample volume was 0.1 dm^3. This resulted in the solution with approximately 1000 mg/dm^3 sample concentration, while the total salt concentration was about 5000 mg/dm^3.

1.3 Selection of the spectral lines used for the analysis

When performing ICP-AES analysis, the various interference effects always have to be taken into account. Since the ICP spectrum is rather rich in spectral lines, spectral interferences may frequently occur [3]. Besides the direct overlapping, heavy background emission may cause problems in many cases. When selecting spectral lines for the analyte elements, care must be taken that the expectable analyte concentration range is rather low, (50–400 mg/kg in the solid sample), which means that sufficiently sensitive lines should be chosen. So that both the interferences, background effects and the sensitivity values could be examined, for both elements, several lines were selected as presented in Table II (with their most important spectral properties).

In case of antimony all the sensitive lines are atom lines with relatively high excitation energies. This is the reason for the fact that no sensitive ion lines can be found for antimony in the visible and ultraviolet range of the spectrum. As for strontium, most of the selected lines are ion lines, since the ionisation energy of Sr is 5.69 eV, which is not very high. Only one atom line can be observed among the Sr lines. Although its excitation energy is the lowest, it is only the fourth regarding the sensitivity values.

Table 2

Selected analyte lines and their key parameters

Line	Wavelength [nm]	Ecxitation energy [eV]	Detection limit [µg/dm^3]	Background eq. conc [µg/dm^3]	Signal/noise ratio
Sb I	187.052	6.63	54.8	1953	0.20
Sb I	206.834	5.99	20.9	1564	0.26
Sb I	217.582	5.70	26 .5	1863	0.21
Sb I	231.146	5.36	45.2	1591	0.25
Sr I	460.733	2.69	3.8	351	1.14
Sr II	216.596	5.72	1.9	128	3.13
Sr II	338.071	3.67	3.9	1129	0.35
Sr II	407.771	3.04	0.12	7.3	55.2
Sr II	421.552	2.94	0.18	13.1	30.4

In Figures 1–3 the spectrum of the selected lines are presented in a ± 0.03 nm range around the peaks.

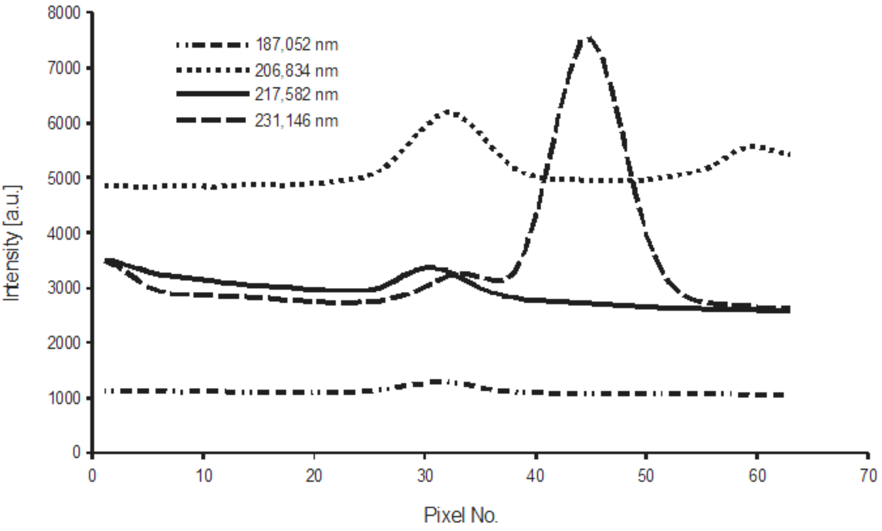

Figure 1. Wavelength scans of the selected antimony lines

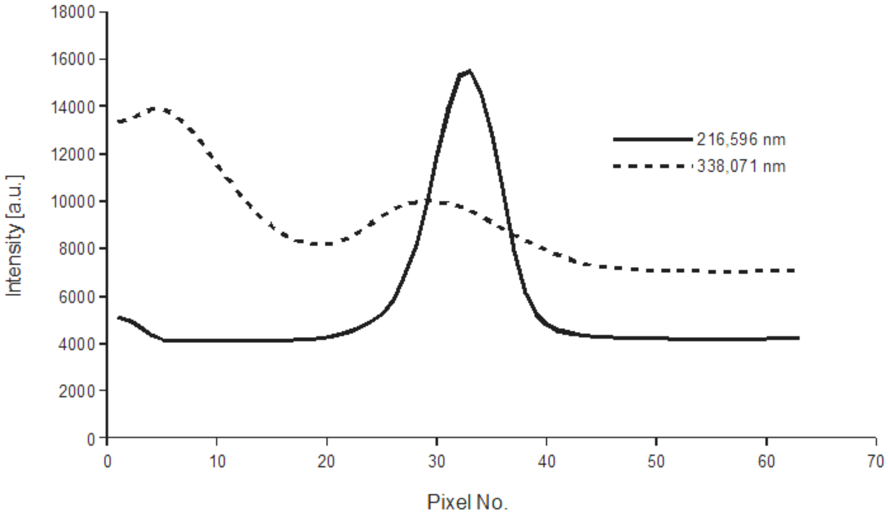

Figure 2. Wavelength scans of the low intensity strontium lines

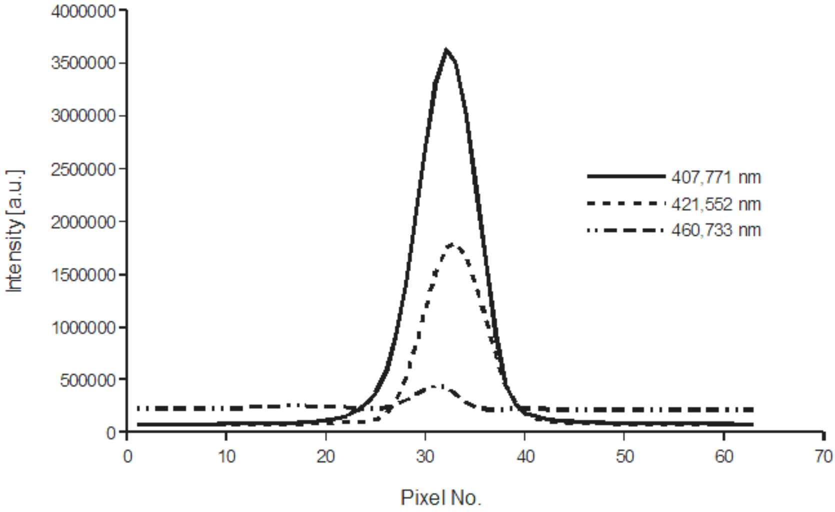

Figure 3. Wavelength scans of the high intensity strontium lines

The spectral properties of the lines were studied using a solution containing 400 µg/dm^3 strontium and antimony, 1000 mg/dm^3 aluminium and all the chemicals used in the course of the sample preparation.

Figures 1–3 and Table II clearly show that the antimony lines are much weaker than those of selected for strontium. Still two of the antimony lines satisfy all the criteria required for the spectrometric determination. The 231.146 nm line seems to be the least suitable because not only due to its low sensitivity but because it suffers from a strong interference caused by a strong line overlapping with the analyte line from right, which may result in inaccurate background correction. The 338.071 nm strontium line also overlaps with an interfering line, and appears to be the least sensitive among the strontium lines.

The radiofrequency power applied to the torch was 1050 W. As for other measurement conditions the details can be found in previous papers [4, 5].

2. Results

In order to obtain some performance characteristics of the method, a real experimental alloy, with a label TA 344 was chosen and five parallel samples were taken out and dissolved using the alkaline method. Following the preparation the antimony and strontium content of the samples were determined in the above-written conditions. One of the samples was selected and measured five times, so that the repeatability of the method could be calculated. The analytical programmes were previously calibrated using matrix-matched calibration solutions prepared from multielement CRM stock solution (Merck Ltd. Certipur IV.). Since the calibration procedure resulted in linear calibration curves for both elements the net intensity values could also be used for calculating the performance characteristics.

Table 3

The data necessary for calculating the repeatability

λ [nm]	Average [mg/dm^3]	SD [mg/dm^3]	RSD [%]	2* RSD [%]
Sb 187.052	0,2275	0,0062	2,73	5,46
Sb 206.834	0,2370	0,0013	0,55	1,10
Sb 217.582	0,2540	0,0083	3,24	6,48
Sb 231.146	0,2245	0,0048	2,14	4,28
Sr 460.733	0,1420	0,0011	0,81	1,62
Sr 216.956	0,1328	0,0004	0,33	0,66
Sr 338.071	0,1386	0,0012	0,90	1,80
Sr 407.771	0,1390	0,0008	0,60	1,20
Sr 421.552	0,1438	0,0019	1,30	2,60

2.1. Calculating the test repeatability

To get the repeatability the results obtained by measuring the same sample solution in five times should be used. The respective data can be found in Table III. Since the measurement data presented in Table III have been measured exactly in the same conditions (the same sample solution, the same analytical programme, the same analyst etc.) the standard deviation values, calculated from the data indicate the repeatability of the measurements. Considering the SD column in Table III it can be observed that except for the 206.834 nm line all the other antimony lines provide poorer repeatability than those of provided by the strontium lines. This fact becomes obvious if the differences in the detection power are taken into account.

2.2 Calculating the reproducibility

Both repeatability and reproducibility is characterised by a standard deviation value. The main difference between the two, is that in case of the latter, something has changed in the course of repeated measurements, for example the samples are taken from the same lot, but they are not perfectly the same, or the determination is carried out by another method or instrument, or the analysis is done by another analyst, etc. In our case five parallel samples have been simultaneously measured to get some information on the effect of sample inhomogeneity. The calculated values are indicated in Table IV.

Table 4

The data necessary for calculating the reproducibility

λ [nm]	**Average [mg/dm^3]**	**SD [mg/dm^3]**	**RSD [%]**	**2* RSD [%]**
Sb 187.052	0.2116	0.0110	5.24	5.46
Sb 206.834	0.2250	0.0098	4.35	8.70
Sb 217.582	0.2550	0.0163	6.40	12.8
Sb 231.146	0.2278	0.0100	4.61	9.22
Sr 460.733	0.1253	0.0045	3.57	7.14
Sr 216.956	0.1342	0.0046	3.43	6.86
Sr 338.071	0.1289	0.0039	3.00	6.00
Sr 407.771	0.1326	0.0037	2.79	5.58
Sr 421.552	0.1376	0.0033	2.38	4.76

Comparing the SD values of Table IV to those of Table III it can be stated that the reproducibility on each wavelength is considerably weaker than the repeatability values, and the effect of the inhomogeneity of the samples cannot be neglected. Since it increases the SD values, the sample inhomogeneity should always be taken into account, especially when the measurement uncertainty it to be determined. As for the analyte elements, the reproducibility of the measurements is poorer on the antimony lines than for the strontium lines. This fact also means that strontium can be determined with somewhat better precision and accuracy.

3. Discussion of the results

The data of the measured detection limits, the repeatability and reproducibility values clearly demonstrate the fact that in case of wet sample preparation, the properties of the sample preparation method has a considerable influence on the performance characteristics of the studied method.

In our case the chemical composition of the base alloy made it necessary to apply the alkaline procedure for the dissolution of the samples. This resulted in sample solutions with rather high salt content, which had several effects on the performance characteristics of the measurements. On one hand it led to deterioration of the detection power, as it could be seen in Table II. The detection limits determined in the sample solutions obtained by the selected sample preparation method are approximately 5–10 times higher than those of measured in aqueous solutions with low salt content. The loss in detection power was much greater for the antimony lines than for the strontium lines. On the other hand the high salt concentration also resulted in high background emission, especially on the antimony lines, which made the background correction more difficult and less accurate and produced poor signal/background ratio.

In Figures 1, 2 and 3 the wavelength scans around the selected spectral lines are presented. As for the antimony lines, it can be stated that the 231.146 nm line is partly overlapped with a high intensity interfering line. This made the background correction especially difficult. Similarly the 338.071 nm strontium line suffers from spectral interference.

The performance characteristics suggest that for antimony the 206.834 nm line is the most optimal. It has the lowest detection limit and it provides the best repeatability and reproducibility values among the antimony lines. As for the strontium the two most sensitive ion line, - 407.771 nm and 421.552 nm, - seem to be the most suitable.

From the data of Table III and Table IV it is also obvious that the precision and accuracy of the measurements are affected by the inhomogeneity of the sample.

Conclusions

In this paper the detailed study of an analytical method for the determination of the antimony and strontium content of AlSi9Cu2,5 type aluminium alloys is presented. Using the suggested sample preparation procedure and applying the spectrochemical parameters determined in the course of our experiments the analysis can be carried out with success.

Acknowledgement

This research was (partially) carried out in the framework of the Center of Excellence of Sustainable Resource Management at the University of Miskolc.

References

[1] Price, W. J.: *Chapters on atomic absorption and fluorescence in Spectroscopy.* McGraw Hill. London, 1969.

[2] Foetisch, M. (Editor): *Plasma Applications.* Volume I. Applied Research laboratoris S. A. Ecublens, 1987.

[3] Záray Gy. (Editor): *Az elemanalitika korszerű módszerei*. (In rough translation: Modern Methods of Elementary Analytics) Akadémiai Kiadó, Budapest, 2006.

[4] Bánhidi, O.: *Examination of the Interference effects in the Course of ICP-AES Determination of Strontium Content of Aluminium Alloys.* XXVI microCAD, University of Miskolc, 29–30 March 2012. Section C, CD-issue of the Conference Publications.

[5] Banhidi, O.: *The Effect of Aluminium and Nickel on Some Spectral Lines of Alkaline Earth Metals in the Course of ICP-AES Analysis*. Materials Science at Uniuversity of Miskolc, edited by Roósz, A. and Tomolya, K. Trans Tech Publications, Materials Science Forum, Vol. 752. pp. 259–267.

Materials Science and Engineering, Volume 39, No. 1 (2014), pp. 15–24.

ADSORPTION OF NONIONIC POLYMERS FROM BINARY MIXTURES AND ITS EFFECT ON THE ELECTROKINETIC POTENTIAL OF AEROSIL PARTICLES

SÁNDOR BÁRÁNY[1]–ATTILA VARGA[2]

A short review on the adsorption of polymer mixtures on the surface of dispersed particles and its relationship with flocculation efficiency is given in this paper. The adsorption of nonionic polyvinyl alcohol (PVA), methylcellulose (MC) and polyvinyl pyrrolidone (PVP) from individual solutions as well as the adsorption of binary mixtures of these polymers on aerosil particles as a function of polymer dose, pH, electrolyte (KCl) concentration and mixture composition has been measured. The adsorption isotherms of these polymers on aerosil particles and their (1:1, 1:3 and 3:1) mixtures show a PVA< MC<PVP sequence of adsorption, testifying the preferential adsorption of PVP from its various polymer mixtures. This is due to effect of hydrophobic interactions between PVP molecules and the surface, on the top of H-bonds formation. The adsorption of PVA, MC and PVP results in a substantial decrease in the electrophoretic mobility of aerosil particles. A correlation between the adsorbed amount of the respective polymers and degree of mobility drop is established. It is also shown that the adsorption of binary polymer mixtures leads to a more pronounced decrease in the zeta-potential than the adsorption of individual polymers. A rise in the "electrophoretic" thickness of the adsorbed layers (calculated from the difference between the zeta-potentials of "bare" and polymer-covered particles) in polymer mixtures compared to the thickness of individual polymer layers has been observed. The laws established were explained by changes of macromolecular conformation in adsorbed mixed polymer layers.

Keywords: nonionic polymers, mixtures, adsorption, adsorption preference, aerosil, particles, electrokinetic potential, polymer layer, thickness, macromolecular conformation.

Introduction and short literature review

Polymers are widely used for flocculation of suspensions in many industrial applications, such as mineral processing, papermaking, water treatment and biotechnology [1]. They can produce large, strong aggregates which can be easily separated by sedimentation, filtration, flotation or centrifugation. The effect of polymers on colloidal stability is mainly due to adsorption of macromolecules onto particle surfaces and to the structure of adsorbed layers formed [2–5]. Flocculation by polymers in most cases is due to the adsorption of a long polymeric chain onto several particles, whereby these particles get linked by polymer bridges ("bridging" flocculation). This is the case for non-ionic polymers, polyelectrolytes of the same charge as the particles or oppositely charged polyelectrolytes with low charge density. The efficiency of particles aggregation/ flocculation increases with the length of loops and tails of the adsorbed macromolecule protruding into the solution, i.e. with the thickness of the adsorbed layer.

---

[1] University of Miskolc, Institute of Chemistry
3515 Miskolc-Egyetemváros, Hungary
akmbsab@uni-miskolc.hu
[2] Transcarpathian II Ferenc Rákóczi Hungarian Institute
Beregovo, Ukraine

Electrokinetic measurements are powerful tools to investigate the structure of interfacial polymer layers [6, 7]. At low ionic strength, the formation of fairly thick hydrodynamically impermeable adsorbed layers of non-ionic polymers shifts the slip plane further into the bulk liquid phase, which causes a decrease in the zeta-potential and hence a reduction in the electrical repulsion between particles with adsorbed polymer. From the difference between the electrokinetic potentials of bare particles and those with the adsorbed nonionic polymer, the 'electrophoretic' thickness of the adsorbed layer can be evaluated (see also below).

The performance of flocculants can in many cases be further improved by applying polymer mixtures due to synergetic effects often occurring in such systems. There have been only limited studies on the flocculating (and stabilizing) capacity of polymer mixtures and its relationship with the adsorption from polymer mixtures and the structure of macromolecular layers on the particles surface. We have performed a study on the adsorption of non-ionic polymer mixtures on a well-characterized aerosil surface and its effect on the electrokinetic potential of the particles. The data were used for the interpretation of the mixed polymer layer structure and flocculation capacity of the corresponding polymer mixtures. Before describing the experimental results obtained, let us inspect the features of adsorption from polymer mixtures – i.e. the first stage of flocculation by polymer mixtures.

Adsorption from polymer mixtures

The analysis of literature data shows that with mixtures of different polymers three major effects should be considered:

- Preferential adsorption of long chains over short ones from solutions of polydisperse polymers (almost always used in practice), even with the same adsorption energy per segment.
- Substitution of weakly bound polymeric segments on the surface by preferentially adsorbed segments of higher adsorption energy within the polymer mixture.
- Complexation of oppositely charged polyelectrolytes in the adsorbed layer.

In dilute solutions of polydisperse polymers, the longer chains are adsorbed preferentially on the surface, since they lose less translational entropy in the solution, while they gain approximately the same (total) adsorption energy [8]. When the surface is saturated with long molecules, plateau adsorption from the mixture remains slightly below the isotherm for isolated molecules. This is due to the much lower solution concentration of long chains in the mixture: the total concentration of the solution is predominantly made up of short chains [8]. The displacement of short chains (which reach the surface more quickly than larger ones) from the surface may take longer time (minutes or hours) than the adsorption process itself. It has been shown by a special electrophoretic method that adsorption equilibrium for polyethylene oxide (PEO) is achieved more rapidly for polymers with very narrow molecular weight (MW) distribution, than for commercial PEO samples with rather broad MW distributions [9].

An adsorbed polymer may be displaced by another if the adsorption energy of the displacer segment(s) is only by 0.01–0.1 kT higher, compared to that of the adsorbed macromolecule. The reason for that is the 'cooperative effect' attributable to the large number of chain segments: the difference in adsorption energy might be small per segment but large per chain [8].

The slow displacement of macromolecules from the surface by molecules with a stronger adsorption capacity has a marked effect on the structure of composite interfacial layers. Csaki and Csempesz [10] have shown that in combination with polyvinyl pyrrolidone (PVP), the adsorption of methylcellulose (MC) molecules on polystyrene (PS) particles is preferred. On silver iodide sol, by contrast, PVP molecules are adsorbed preferentially against MC molecules [11].

The thickness of the adsorbed polymer layer is one of the key factors determining the effectiveness of uncharged polymers in flocculating and stabilizing colloidal dispersions. It has been shown by photon correlation spectroscopy and laser Doppler electrophoresis that the thickness of methylcellulose layers on polystyrene and silver iodide surfaces was about twice as high as that of PVP, with a wide concentration range of the polymers in the solution [12]. No differences in the thickness of individual polymer layers on PS surfaces from 1 h to 24 h adsorption periods could be detected. However, a definite rise in the thickness of the MC-PVP layer on PS and some decrease of this polymer mixture layer on AgI could be observed after longer contact time [11, 12]. These features can be ascribed to a slow displacement of the PVP molecules from the polystyrene surface by MC molecules with a stronger adsorption capacity.

Based on the adsorption data of non-ionic polymer mixtures and their effect on the aggregation of sol particles, Csempesz and co-authors [12, 13] suggest that in the case of polymer mixtures, the conformation of adsorbed macromolecules on the surface is significantly altered: preferentially adsorbed segments tend to substitute weakly bound polymeric segments in the surface layer. As a result, the length of loops and tails formed from the latter is likely to increase. Lee and Liu [14] also assumed that the adsorption of mixed polymers on particles surface generates an extended confirmation of polymers. This enhances the formation of polymeric bridges between the particles and consequently, stimulates flocculation efficiency. Somasundaran [15] has shown that the flocculating activity of polyelectrolyte (PE) mixtures depends on the size of polymers, their charge density and the dosing sequence. Enhanced flocs or “superflocs” were formed through polymer-polymer complexation [16].

1. Materials and methods

As adsorbent “Highsil” grade aerosil particles with a specific surface area of 180 m^2/g has been used. The nonionic polymers of polyvinyl alcohol with M 20,000 (2% acetate groups), polyvinyl pyrrolidone with M 24,000 and methylcellulose with M 84,000 were applied. The adsorbed amount (Γ) was determined after contacting the polymer solution with the adsorbent at room temperature (25 $^{\circ}C$) for 24 hours. As preliminary tests showed, this contact time was enough to reach adsorption equilibrium. The amount of adsorbent in each sample was 0.5 g, and the volume of the solution was 50 cm^3. Once the solution had reached equilibrium, it was separated from the solid by applying 30 min centrifugation time at speed of 20,000 rpm. The concentration of polymers in the solution was determined by interferometer or colorimetric measurements (from the intensity of light transmitted by the solution of coloured complex compounds of PVA) using calibration curves as described in papers [17, 18]. The electrophoretic mobility of the particles were measured using a Brookhaven Zeta Sizer Instrument .

At this point, we have to emphasize that it is actually impossible to calculate the exact value of the ζ-potential of soft particles built up of a hard core with adsorbed polyelectrolytes on it, despite all recent progress/ developments in the theory of electrical double layers in such systems. In fact, the values of the electrokinetic potential given below represent some "efficient" ζ-potentials equal to the electrophoretic mobility multiplied by the ratio of the viscosity of the medium to its permittivity. As shown in the literature, this calculation method is worldwide accepted, and serves as a basis for the calibration of Zeta Sizer instruments.

2. Results and discussion

2. 1. Adsorption measurements

The results of adsorption measurements for individual polymers and their binary mixtures are presented in Figures 1–3. At low equilibrium concentrations, the adsorption isotherms are characterized by a stepwise rise, with tendency to reach saturation at high concentrations (Figure 1). These differ from the "high-affinity" type isotherms, which are characterized by total extraction of the added polymer at low contents, thus fast reaching plateau adsorption with high polymer concentrations, and which are typical for the polymers studied on hydrophobic surfaces [8, 19]. The maximal adsorbed amount reaches several dozens of mg/g, i.e. 0.1–0.2 mg/m^2, which is less than the values typical for nonionic polymers adsorbed onto solids (about 0, 5–1,0 mg/m^2, see [8, 19]). This might be due to the fact that the adsorbed amount is calculated with respect to the total surface area, S (determined by the adsorption of argon using BET method) instead of the surface area really accessible for macromolecules. The latter is much less than S_{total} because of the aggregation of primary particles.

Figure 2 shows that with rising pH, the adsorption of PVA and MC decreases. This can be explained by a decrease of the number of non- dissociable OH group on the silica surfaces, which are able to form H-bonds with hydroxyl groups of the respective polymers. H-bond formation onto the silica surface is the main adsorption mechanism of these compounds [19, 20]. The participation of water molecules and hydrated counter-ions in forming adsorption bonds between macromolecules and the silica surface is also supposed [19]. At the same time, the adsorption of PVP does not change substantially with an increase (from 3 to 9) in the pH of the medium, and a marked decrease in adsorption is observed only at pH > 11.

According to the authors [20], the formation of H-bonds between non-dissociable OH groups on the surface and tertiary amino-groups of PVP may lead to a proton transfer from the silanole group to the adsorbate, resulting in formation of VP…H^+ type ions.

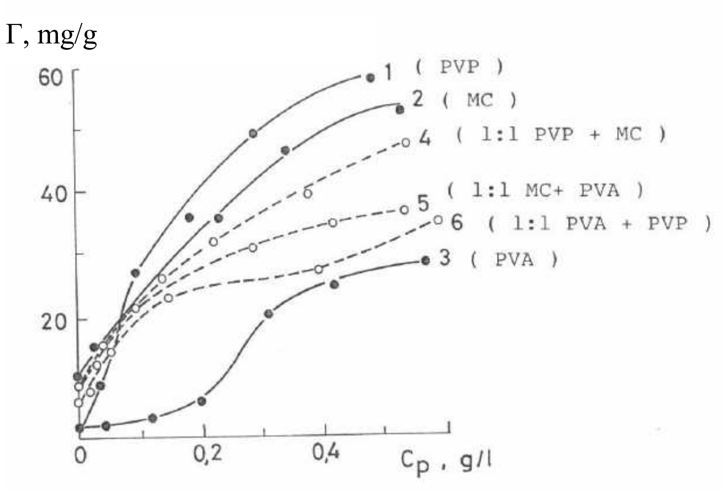

Figure 1. Adsorption isotherms of PVP (1), MC (2), PVA (3) and of the 1:1 binary mixtures of PVP+MC (4), MC+PVA (5), PVA+PVP (6) adsorbed on the surface of aerosil particles at pH 7.4. The summed concentration of polymers in the mixture and the summed adsorption of polymers in mixture are indicated

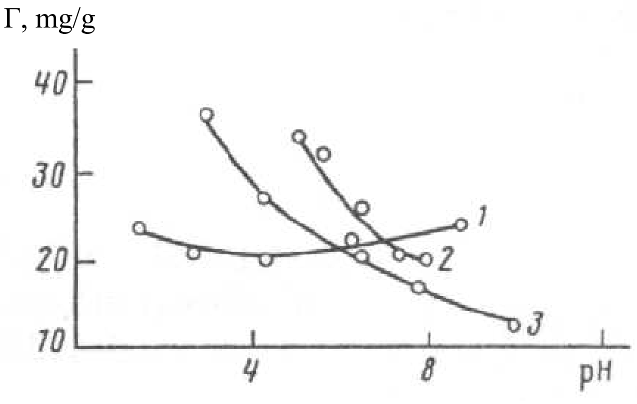

Figure 2. Dependence of PVP (1), MC (2) and PVA (3) adsorbed amount on aerosil particles on the pH of the solution. KCl concentration =5x10^{-3} mol/l

The adsorption of the polymers studied decreases in the following series: PVP>MC>PVA, which is different from the sequence of adsorption of these polymers onto AgI surface [20, 21]. The steepness of the rising part of the isotherms, characterizing the affinity of the macromolecules to the surface, for PVP and MC is also higher than that of PVA. This means that PVP will displace the adsorbed MC and, especially PVA molecules from the surface, and the first compound should adsorb from the polymer mixture preferentially.

Figure 1 also shows that the total adsorption of a 1:1 (by mass) polymer mixture is less than the sum of the adsorbed amount of individual components. Obviously, this phenomenon is due to competitive adsorption of polymers from their mixture which results in suppression of adsorption of one polymer by the other one. The degree of such suppression is different in various mixtures. For example, the summed adsorption in a 1:1 mixture of MC+PVA at polymer concentration of 0.4 mg/dm^3 is 33 mg/g (Figure1), while with "half" concentration of the same polymer (0.2 mg/dm^3), MC adsorption reaches 35 mg/dm^3, and the adsorption of PVA reaches even 40 mg/dm^3. The adsorption of PVP and PVA from individual/separate solutions at 0.2 mg/dm^3 is 37 mg/g and 5 mg/g, respectively, while the summed adsorption of these polymers from the same 1:1 mixture reaches only 25 mg/g, i.e. slightly more than the half of $\Gamma_1 + \Gamma_2$. Similar results have been obtained for a PVP+MC mixture.

The suppression of non-ionic polymer adsorption by other polymers is confirmed by the isotherms of adsorption of individual polymers from their binary mixtures (Figure 3). The content of a selected polymer in the presence of a second polymer was determined by colorimetric method. It can be seen that PVP is adsorbing preferentially from 1:1 PVP+PVA mixtures; its adsorption exceeds the adsorbed amount of PVA by 2–2.5 times in a wide range of mixture concentrations. This is in line with a steeper rise in the initial section of the isotherms for PVP, as compared to those of PVA (Figure 1). Analogous results have been obtained for 1:1 mixtures of PVP+MC and for polymer mixtures with a 2:1 or 3:1 ratio of the components.

The preferential adsorption of PVP from its mixtures with other polymers is further confirmed by data on substitution of polymers by other polymers from the adsorbed layer. Table 1 shows that changes in the order of adding the components in the polymer mixture, i.e. first PVP, and 6 h later PVP or, inversely, PVA first, then PVP, does not substantially change the adsorption of polyvinyl-pyrrolidone. On the other hand, the introduction of PVP as the second component of the system, will lead to the substitution of considerable amounts of pre-adsorbed PVA, while addition of the latter does not influence the adsorption of PVP substantially. The firm binding of PVP molecules to the surface might be promoted – besides H-bond formation – by hydrophobic interactions taking place between the hydrocarbon parts of the molecule and the hydrophobic parts of the silica surface.

The preferential adsorption of MC in its mixtures with PVA is the least pronounced, as it can be deduced from the data presented in Table 1.

It has also been shown that increasing the electrolyte (KCl) concentration, the adsorbed amount of the studied polymers under decreases. This type of behavior was observed in a number of dispersions containing non-ionic polymers [19], and was explained by the influence of several factors, such as the competitive adsorption of ions and polymeric segments on the surface, ion-dipole interactions between counter-ions and dipoles of the macromolecule repeated unit, changes in the structure of the electric double layer etc. (see in detail [19]).

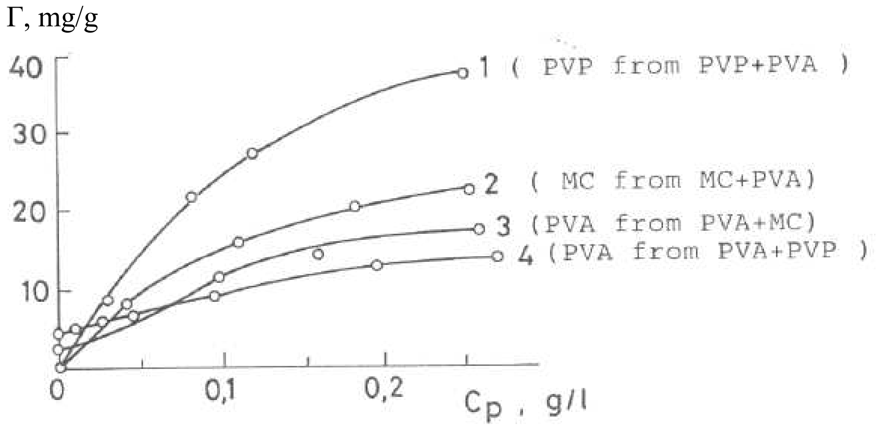

Figure 3. Adsorption isotherms of (1) PVP from its 1:1 mixture with PVA, (2) of MC from its mixture with PVA, (3) of PVA from its mixture with MC and (4) of PVA from its mixture with PVP (4). The equilibrium concentration and adsorption of individual polymers from their mixture with other polymer are shown

Table 1

Absorbed amounts (mg/g) of non-ionic polymers and their 1:1 mixture on aerosil particles

Initial conc	**PVP+PVA**		**Initial conc**	**MC + PVA**	
g/l	Γ_{PVP} at addition of PVP		g/l	Γ_{MC} at addition of MC	
	first	second		first	second
0,1	12,8	8,1	0,063	4,1	2,4
0,2	23,0	17,4	0,125	6,2	3,5
0,4	32,0	27,9	0,25	13,3	6,3
0,8	43,8	35,6	0,5	21,0	12,1
			0,8	26,6	15,5

2. 2. Electrokinetic aspect of polymer mixture adsorption

The adsorption of PVA, MC and PVP results in a substantial decrease of the electrophoretic mobility of aerosol particles (Figure 4). There is a good correlation between the adsorbed amount and the degree of mobility drop: the higher the adsorption is, the more pronounced the decrease in mobility will be (compare Figures 1 and 4). The reason for

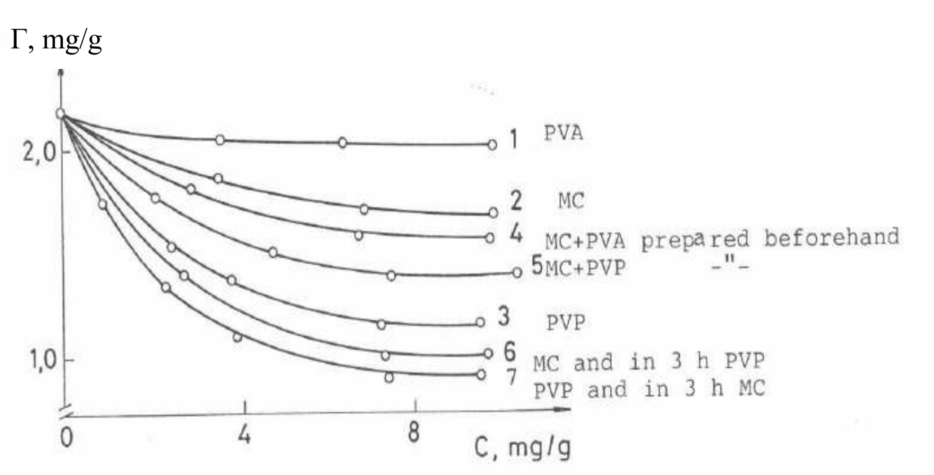

Figure 4. Electrophoretic mobility of aerosil particles plotted against polymer content in the following suspensions (calculated for 1 g of adsorbent): (1) PVA, (2) MC, (3) PVP, (4) pre-prepared MC+PVA mixture, (5) pre-prepared MC+PVP mixture, (6) MC+PVP mixture, with a subsequent addition of MC and PVP (3 hours later), (7), PVP+MC mixture with a subsequent addition of PVP and MC (3 hours later)

that is the following: at low ionic strength, adsorbed non-ionic polymers form fairly thick hydro-dynamically impermeable adsorbed layers, which shift the slip plane further into the bulk liquid phase, causing a decrease in the zeta-potential. Supposing that neither the surface charge density, nor the distribution of ions in the double layer is substantially changed by polymer adsorption [19], the hydrodynamic thickness of the adsorbed polymer layer *h* can be calculated from the well known relationship describing the electric potential distribution in the diffuse double layer:

$$\exp(\kappa h) = \tanh(ze\zeta/4kT)/(ze\psi_\delta/4kT)$$

where: κ – is the reciprocal Debye length, h – is the thickness of the diffuse layer between the boundary of the Stern-layer and the shear plane, ζ – the electrokinetic potential of the particle at a given h value, ψ_δ – the Stern-potential, equalized to the value of zeta-potential value of initial, polymer-free particles (ζ_0).

According to the above formula, the thickness of the polymer layer is $d = h+\delta$ (where δ – is the thickness of the Stern layer ≈ 0.4 nm), i.e. the distance from the surface to the point where the viscosity of the liquid changes dramatically. It can be also seen that the adsorption of binary polymer mixtures leads to a more pronounced decrease in the zeta-potential than the adsorption of individual polymers. This is typical for example for PVP+MC mixtures (Figure 4). It is interesting to note that with a subsequent addition of polymers (as mixture components), the decrease in zeta is bigger (see curves 6 and 7 in Figure 4) than with the addition of a pre-prepared mixture (see curve 5).

The maximum values of adsorbed layer thickness calculated using the above expression were 4 nm for PVA, 6 nm for MC, 12 nm for PVP, 8 nm for pre-prepared MC+PVA mixture, 10 nm for a pre-prepared PVP+MC mixture, 16 nm for a mixture of MC+PVP (where PVP was added 3 hours later than MC), and 17 nm for MC+PVP mixture (where MC was added 3 hours later than PVP).

So, in line with electrophoretic and adsorption measurements, the calculated layer thickness of some polymer mixtures will exceed the thickness of individual polymer layers.

In good agreement with the adsorption data of polymers from their binary mixtures, the sequence of addition of the mixture components has practically no effect on the electrophoretic mobility of particles (see curves 6 and 7 in Figure 4). According to the described adsorption measurements, the total adsorbed amount of a mixture is less than the sum of adsorbed amounts obtained separately for the mixture components (see above) in solutions of the same concentration. Consequently, the more pronounced drop in mobility in the presence of the polymer mixture is not deriving from the increased adsorption of the mixtures but rather relates to conformational changes of macromolecules in the adsorbed layer. It can be supposed that the adsorption of PVP with high affinity to the surface ends up with the in occupation of the majority of “adsorption active” surface centers. This creates obstacles for the adsorption of a second polymer, i.e. adsorbed PVP molecules will inhibit most surface contacts. As a consequence, PVA or MC adsorption from various mixtures with PVP will take the form of long loops and tails, with a relatively small number of surface contacts, which is the reason for the sharp decrease in the electrophoretic mobility of particles.

Acknowledgement

This research was (partially) carried out in the framework of the Centre of Excellence of Sustainable Resource Management at the University of Miskolc.

References

[1] Moody, G. M.: *Polymeric flocculants*. In: Williams P. A. (editor). Handbook of industrial water soluble polymers. Oxford: Wiley–Blackwell; 2007, Chapter 6. p. 134.
[2] Vincent, B.: *Adv. Colloid Interface Sci*. 1974; 4:193.
[3] Baran, A. A.: *Usp*. Khim. 1985; 54:1100.
[4] Gregory, J.: *Polymer adsorption and flocculation*. In: Finch CA, (editor). Industrial water soluble polymers. Cambridge: Royal Society of Chemistry; 1996, p. 62.
[5] Fleer, G. J.: *Scheutjens JMHM. Modeling polymer adsorption, steric stabilization and flocculation*. In: Dobias B. (editor). Coagulation and flocculation. New York: Marcel Dekker; 1993, p. 209.
[6] Koopal, L. K.–Lyklema, J.*: Faraday Discuss*. 1975; 59:230.
[7] Baran A. A.: *Platonov BE. Usp.* Khim. 1981; 50:161.
[8] Fleer, G. J.–Cohen-Stuart, M. A.–Scheutjens, J. M. H. M.–Cosgove, T.–Vincent, B.: *Polymers at interfaces*. London: Chapman & Hall; 1993.
[9] Chaplain V.–Janex, M. L.–Lafuma, F.–Graillat, C.–Audebert, R.: *Colloid. Polym*. Sci. 1995; 273:984.
[10] Csaki, K. F.–Csempesz, F.: *Colloids Surf.* A. 2001; 190:3.
[11] Mitina, N. S.–Baran, A. A.: *Ukr. Khim*. Zh. 1990;56:578.
[12] Csempesz, F.: *Chem*. Eng. J. 2000, 80:43.

[13] Csempesz, F.–Rohrsetzer, S.: *Colloids Surf*. 1988, 31:215.
[14] Lee, C. H.–Liu, J. C.: *Adv. Environ*. Res. 2001, 5:129.
[15] Somasundaran, P. X.: *Colloids Surf. A.* 1993, 81:17.
[16] Somasundaran, P. X. J.: *Colloid Interf. Sci*. 1996, 177:237.
[17] Horacek, J.: *Chem*. Prum. 1962, 12:385.
[18] Eremenko, B. V.–Platonov, B. E.–Polischuk, T. A.: *Ukrainian Chem. J.* 1978, 44:901.
[19] Bárány S.: *Polimerek diszperz rendszerekben, A Kémia újabb eredményei*. Akadémiai Kiadó, Budapest, 2000, pp. 1–144.
[20] Eremenko, B. V.–Baranchuk, N. D.–Malysheva, M. L.: *Colloid J.* 1985, 47:678.
[21] Csempesz, F.–Rohrsetzer, S.: *Colloids a. Surf*. 1984, 11:173.

Materials Science and Engineering, Volume 39, No. 1 (2014), pp. 25–29.

USING ENERGY DISPERSIVE X-RAY FLUORESCENCE TECHNIQUE TO SUPPORT REFLOW SOLDERING TECHNOLOGY

DÁNIEL KONCZ-HORVÁTH[1]–ZOLTÁN GÁCSI[2]

There are several parameters affecting the reliability of solder joints (e.g. surface finish), therefore, an optimal time-temperature profile should be determined for the proper control of void and intermetallic compound (IMC) formation during the reflow process. Since IMCs are most frequently formed in Sn-Ag based lead-free solders, the amount of these must be taken into account. In this paper, the effects of different peak temperatures on the ED-XRF measurements of major metallic elements (e.g. Pb contamination) in soldered pads were studied. Results measured at extremely high peak temperature demonstrated that the intensive dissolution of the Cu pad yields large Cu_6Sn_5 IMCs in the bulk solder.

Keywords: ED-XRF, reflow, lead-free, void, intermetallic.

Introduction

Reflow soldering process (whereby solder paste is applied) is a mainstream interconnect technology, due to its productivity and reliability [1]. The so-called surface mount technology (SMT) consists of three main steps, including the printing process of the paste (a mixture of solder powder and flux), stepwise mounting and a final melting (reflow) phase. The whole process is similar to conventional eutectic solder reflow processes; however, the applied temperatures are different [2]. The described soldering process can be optimized by carefully selecting the properties of the applied flux and the solders. Voids can be characterized by non-destructive (e.g. 2D X-Ray) analysis [3], while IMCs can be observed with destructive methods (e.g. cross-section photos). One of the aims of this study was to examine the applicability of non-destructive ED-XRF analysis for the classification of solder joints.

X-ray fluorescence is a simple and fast non-destructive method of homogeneous (mechanically inseparable) materials [4]. Nowadays, one of the main applications of the XRF technique is the testing of RoHS (Restriction of Hazardous Substances, 2002/95/EC) elements in electronic products [5]. Generally, the microstructure of the bulk material after the reflow process is not homogeneous, but the results of XRF measurements are in good agreement with the required standards of average metallic compositions.

---

[1] University of Miskolc, Institute of Physical Metallurgy, Metalforming and Nanotechnology
3515 Miskolc-Egyetemváros, Hungary
femkhd@uni-miskolc.hu
[2] University of Miskolc, Institute of Physical Metallurgy, Metalforming and Nanotechnology
3515 Miskolc-Egyetemváros, Hungary
femtangz@uni-miskolc.hu

1. Experimental procedure

The experiments were conducted on six pieces of printed circuit boards (PCB). Each PCB had 10 pads with a 4x5 mm^2 tinned surface. These samples were prepared by paste printing (95.5wt%Sn–4wt%Ag–0.5wt%Cu alloy powder mixture with 10% flux) and with a heating process applied. The thickness of print deposition was about 150 µm, which ensured an infinitely thick layer for XRF analysis. The temperatures of the experimental heating profiles can be seen in Table 1 – with the same values set for all cases in the preheating zones (1–5) to ensure the best activation of flux. The temperatures of the peak zones (6–7) T_{PEAK} were set at three different levels (low, normal, high), including extreme cases. The transport speed in the reflow oven was kept constant (800 mm/minutes).

Table 1

*Temperatures of the reflow oven**

	Zone temperatures, °C						
Profile	1	2	3	4	5	6	7
Low	130	150	177	197	225	230	230
Normal	130	150	177	197	225	250	260
High	130	150	177	197	225	275	280

**N_2 inert gas atmosphere was used*

XRF measurements were performed with a Fischerscope X-ray XDAL spectrometer operating at 50 kV. The X-ray fluorescence spectra were collected by using a silicon PIN detector with high energy resolution (<200eV). The samples were measured for 180s, using the utmost collimator (0.6 mm diameter). WinFTM (Windows-based) v.6.20 software with a ‘fundamental parameters method’ installed on it has been used for computation.

Phoenix PCBA 2D X-Ray equipment was used for performing and evaluating 2D X-Ray measurements with a Vintage software. After 2D analysis, image processing of the X-Ray photos was done with Leica QWin Pro 2.3 software. Observations of the microstructures (on cross-sections) were made using Scanning Electron Microscopy (AMRAY 1830I) equipment. All measurements were carried out on the reflowed bonds.

2. Results and discussion

10 points on each profile were selected for the XRF measurements. The measured concentrations in Figure 1 show that the amount of Cu (1,92±0,51wt%) is twice higher for the normal than for the low-temperature case (0,99±0,17wt%), which indicates increased Cu-dissolution from the PCB pad.

The relative standard deviation (RSD,%) of Cu increased with temperature. Normally, the RSD values of the respective elements (Ag, Cu and Pb) were lower than 20 percent. Wherever Cu-dissolution passed the threshold value [6], large Cu_6Sn_5 IMCs (about 30–50 µm) were formed in the bulk solder at random positions (see Figure 2). It is important to note that larger IMCs make the bonds less reliable [1], and influence the dispersion of other elements such as Pb. The size of IMCs were 1–5 µm in the bulk solder at normal case. IMC layers were also measured in the cross-section images. 3,2±0,5 μm, 5,1±1,0 μm and 6,7±1,6 μm were found, from low to high $T_{PEAKs.}$

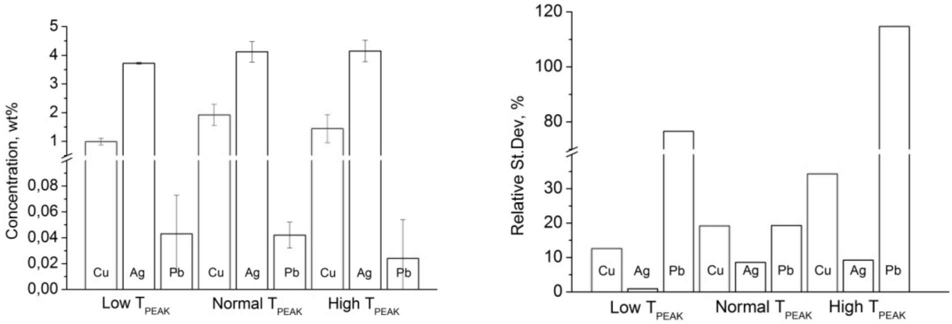

a) b)

Figure 1. Measured concentrations of Cu, Ag and Pb elements – a) mean values – b) RSD values

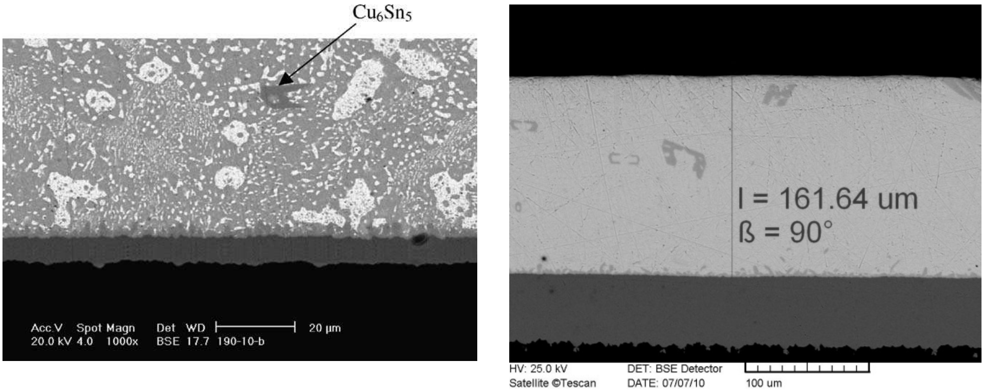

a) b)

Figure 2. IMCs in bulk solders – a) eutectic Sn-Pb (after 10 min reflow at 190°C [6]) – b) Sn-4Ag-0.5Cu after high T_{PEAK} (experimental result)

Based on Yunus's [3] and Harris's [7] study on void formations in Sn-Ag-Cu solder alloys on Cu substrate, it can be seen that the characterization of voids is not negligible. Therefore, the count and area parameters of the voids were determined with a special image analysing process (Figure 3). Grey images were transformed into binary images with the help of 'greyscale levels effect' (the voids segregated from their background), then the detected objects were measured.

While there were no significant differences among maximum void diameters (22±3 μm; 25±3 μm and 24±3 μm from low to high T_{PEAKs}), the area (3,0±0,3%; 1,9±0,2%; 1,1±0,2%) and count number (92±14 pcs; 43±3 pcs; 28±3 pcs) of the voids strongly depended on temperature. It can be stated that at low T_{PEAK}, the dispersion of Pb in bulk solder correlated with void formation. Measurement uncertainty for Pb was the smallest by normal T_{PEAK} profiles, due to the most homogeneous microstructure of the bulk solder.

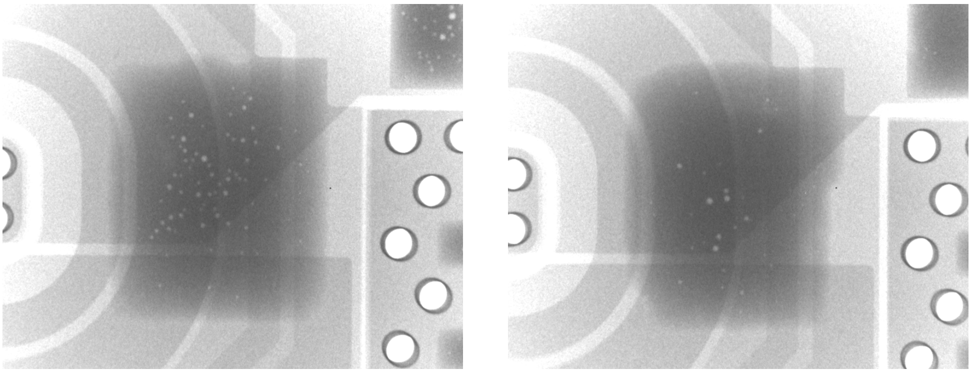

a) [2,4%, 69 pcs, $d_{max} = 22\mu m$] b) [1,3%, 30 pcs, $d_{max} = 22\mu m$]

Figure 3. Characteristics of voids [area fraction; count number; maximum diameter] in bulk solders – a) at low T_{PEAK} – b) at high T_{PEAK}

Conclusion

The prepared PCB samples were reflowed using three different time-temperature profiles, and, after the application of different heating processes, measured with ED-XRF technique. Based on the results, it can be stated, that the relative standard deviations of Cu, Ag and Pb strongly depended on the applied peak temperatures. At low temperatures, void formation had a significant effect on RSD values. Comparing the values obtained at high temperatures to those of the normal case, it can be concluded that large IMCs entail increasing RSD values. We therefore suggest a potential classification scheme applicable to reflow soldered joints, as presented in Table 2.

Table 2

Potential classification scheme

Element	**Relative St.Dev., %**		
Cu	<20	<20	>20
Pb	>20	<20	>20
Classification	Multiple voids	Normal process	Large IMCs

Acknowledgements

The authors would like to express their gratitude to Árpád Kovács for the SEM examinations and Erika Szurokné for the experimental support. The research work presented in this paper was based on the results achieved within the TÁMOP-4.2.1.B-10/2/KONV-2010-0001 project and carried out as part of the TÁMOP-4.2.2.A-11/1/KONV-2012-0019 project in the framework of the New Széchenyi Plan. The realization of this project is supported by the European Union, and co-financed by the European Social Fund.

References

[1] Alex, C. K. S.–Chan, Y. C.: *Reliability Studies of Surface Mount Solder Joints* – Effect of Cu-Sn Intermetallic Compounds, IEEE Transactions on Components, Packaging, and Manufacturing Technology, Part B. Vol. 19, No. 3 (1996), pp. 661–668

[2] Lee, N-C.: *Reflow Soldering Processes and Troubleshooting* SMT, BGA, CSP and Flip Chip Technologies, first ed., Newnes, USA, 2002.

[3] Yunus, M.–Srihari, K.–Pitarresi, J. M.–Primavera, A.: *Effect of voids on the reliability of BGA/CSP solder joints.* Microelectronics Reliability 43 (2003), pp. 2077–2086.

[4] Rößiger, V.–Nensel, B.: *Analyse von Schichtdicken mit Röntgenfluoreszenz*. Jahrbuch Oberflächentechnik, Leuze Verlag, Bad Saulgau, (2004), pp. 195–225

[5] P. Cusack–T. Perrett: *The EU RoHS Directive and its implications for the plastics industry*. J. Plastics, Additives and Compounding, Vol. 8, Iss. 3, (2006), pp. 46–49.

[6] Sharif, A.–Chan, Y. C.–Islam, R. A.: *Effect of volume in interfacial reaction between eutectic Sn-Pb solder and Cu metallization in microelectronic packaging*. Materials Science and Engineering B106 (2004), pp. 120–125.

[7] Harrison, M. R.–Vincent, J. H.–Steen, H. A. H.: *Lead-free reflow soldering for electronics assembly*. Soldering & Surface Mount Technology, 13/3 (2001), pp. 21–38.

Materials Science and Engineering, Volume 39, No. 1 (2014), pp. 31–40.

QUANTITIVE ANALYSIS OF AIR POLLUTANTS PRODUCED FROM THE COMBUSTION OF HEAVY METAL CONTAMINATED TREES IN DIFFERENT COMBUSTION EQUIPMENTS

HELGA KOVÁCS[1]–KATALIN SZEMMELVEISZ[2]–TAMÁS KOÓS[3]

One of the most widely used in-situ remediation methods is phytoextraction, during which excessive amounts of heavy metals are removed from the soil by plants capable of storing and uptaking contaminants. However, the combustion of these plants assumes that their heavy metal content is transformed into gaseous and solid combustion matter. Therefore, extensive research is required to define the composition of such hazardous remains and to identify the proper methods for the treatment and disposal of the waste. In this article, we examine the gaseous and solid pollutant particle content of the flue gas produced from combustion, as well as the heavy metal content of the fly ash. We have developed two different experimental processes applicable to domestic-scale and semi-plant scale biomass combustion, respectively. Oak and poplar samples from a heavy metal contaminated site were used for both experiments. The domestic-scale test was conducted with a furnace of 7 kW heat capacity, with closed combustion chamber; the semi-plant scale examination was carried out in a 500 MW capacity boiler equipped with an automatic fuel feeding system and a cyclone dust extractor. In both combustion experiments, the composition of flue gas was measured with a portable gas analyser type HORIBA PG-250. For the analysis of the heavy metal content of the fly ash, DX4 EDAX EDS microprobe by an AMRAY 1830 type scanning electron microscope and ICP-AES tests by a 720 ES instrument were applied.

Based on our results, it can be determined, that any type of combustion device used for burning biomass from heavy metal polluted sites (brownfield lands) must allow the separation of the fly ash from the flue gas, and make the proper handling of the solid burning residues viable.

Keywords: brownfield lands, ligneous plants, heavy metal pollution, combustion experiments

Introduction

Constant population growth and large-scale pollutant emissions from intensive industrial activities set ever demanding challenges to mankind – especially from an ecological point of view. Pollutants emitted into the environment often cause irreversible damage. Over the past few decades, decontamination efforts have gained special importance in Eastern-European countries such as Hungary. The industrial changes of the early 90's lead to the transformation of old, obsolete structures and significantly reduced the role of heavy industry in sectors like metallurgy, mining and machinery. Abandoned industrial sites gradually turned into

---

[1] University of Miskolc, Institute of Energy and Quality Affairs
3515 Miskolc-Egyetemváros, Hungary
tuzkh@uni-miskolc.hu
[2] University of Miskolc, Institute of Energy and Quality Affairs
3515 Miskolc-Egyetemváros, Hungary
tuzszemt@uni-miskolc.hu
[3] University of Miskolc, Institute of Energy and Quality Affairs
3515 Miskolc-Egyetemváros, Hungary
koostamas87@gmail.com

brownfield lands along the years. The reutilization of these areas cannot be achieved without decontaminating the polluted fields.

In the case of polluted lands, especially soils with high heavy metals contents, a common method for remediation is phytoextraction [1], through which the heavy metals present in the soil get accumulated in the plants' tissues [2–5]. Once in-situ remediation get accomplished, these plants are still suitable for energetic utilization, supposing that no heavy metal components accumulated in the plant will cause damage to the environment. A substantial fraction of the heavy metal content of the biomass fuel can be found in the ash after burning, while a smaller fraction will enter the flue gas, in gaseous and solid form. In this paper, we examine the solid and gaseous air pollutants formed in the flue gas during the combustion of such fuels. For purposes of our investigations, we have taken oak and poplar samples from a closed mining site in Hungary.

The energetic use of ligneous plants highly depends on the combustion technology applied and the type of the combustion equipment used. During our research, we first examined the domestic utilization of firewood contaminated with heavy metals. In Hungary, manually-fed combustion devices of low capacity are common, which means that the burning process takes place under relatively uncontrolled circumstances. Therefore, we used an experimental furnace to determine combustibility. The main objective of the combustion experiment was to examine the emission of the solid and gaseous air pollutants produced, and to sample the fly ash formed in the burning process. We have conducted laboratory measurements to define the composition of the fly ash.

After having completed the domestic-scale combustion experiments, we examined the change in the amount of emitted pollutants under controlled circumstances, in a 500 kW capacity boiler.

The underlying question of our investigations was whether it is possible for heavy metal contaminated ligneous plants taken from brownfield lands to be transformed into commercially viable fuels appropriate for energetic utilization?

1. Combustion experiments

We have carried out two combustion experiments for the examination of ligneous plants contaminated with heavy metals. We have used oak and poplar samples from the same site for both the domestic-scale and the semi-plant scale experiments.

1.1. Domestic Domestic-scale combustion experiments

The simplest method for the energetic utilization of contaminated biomass would be to burn the logs obtained from the polluted sites in household or industrial combustion units, in the nearest town. In order to determine whether the respective heavy metal contaminated biomass is suitable for residential utilization, combustion experiments have been carried out. The tests were conducted with a furnace of 7 kW capacity, with closed combustion chamber.

The scheme of the measurement system is shown in Figure 1. Two sampling points have been allotted on the straight flue gas conduction tube, at the outlet of the boiler. One set of samples, for solid air pollutant analysis, were taken at the first point, while another set for flue gas composition analysis were taken at the second. In the case of traditional, manually-fed household combustion devices, the soot content of the flue gas usually increases after feeding. In order to replicate a realistic combustion process, some flue gas samples were taken during fuel feeding, so some of the values represent this “sooting” stage.

In Hungary, no specific emission limit values for household combustion devices have been set by governmental regulations so far, but, considering recent EU environmental directives, this will undoubtedly change in the near future. The lack of regulations makes it unclear whether heavy metal contaminated biomass can be burnt uncontrollably in household devices. Aim of our researches was to develop a model that resembles “uncontrolled residential utilization” as closely as possible.

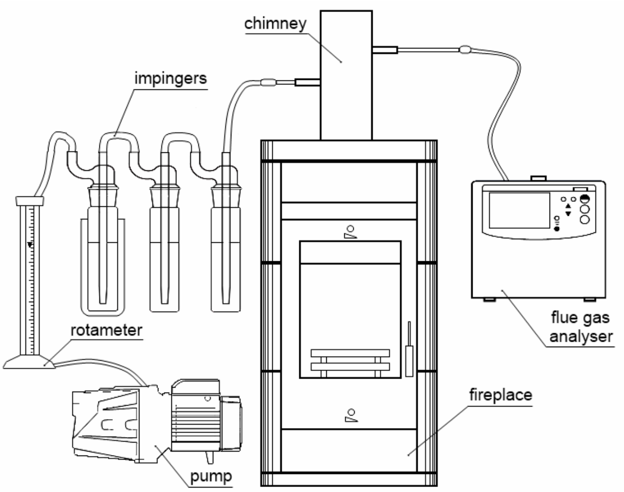

Figure 1. Scheme of the measurement system (domestic-scale experiment)

1.2. Semi-plant scale combustion experiment

The semi-plant scale experiment was carried out in a 500 kW capacity boiler with an automatic fuel feeding system (Figure 2). The boiler is equipped with a cyclone dust precipitator. The gaseous pollutant content and the fly ash concentration of the flue gas produced from the combustion process has been examined by setting up a standard sampling point in the upper part of the chimney. For the analysis of solid particles flowing in the flue gas, we have taken samples from the fly ash collected by the cyclone, then from the fly ash leaving the chimney together with the flue gas.

Figure 2. Photo of the examined boiler (semi-plant scale experiment)

2. Examination of pollutant emission

2.1. Gaseous pollutants

We have examined the composition of the flue gas produced from the above described combustion experiments with a portable gas analyser type HORIBA PG-250, which allows the determination of flue gas components along the following measurement principles. Based on a chemiluminescence method, CO and SO_2 were determined through infrared absorption by a NO_x analyser (inside the device). The analyser is supplied with two pyroelectric sensors. One of them is to measure CO_2 absorption, the other is the reference sensor, whereby different wavelengths are applied to induce CO_2 absorption and to determine light energy, respectively. Actual measurement is made with an analysing zirconium-oxide sensor. The applied measurement methods comply with all standard regulations [6–11]. As for/considering gaseous air pollutants, the measured values should be converted to a given oxygen concentration according to the relevant regulations [12–13]. KöM Decree No. 23/2001. (XI.13) sets a reference value of 11% oxygen content for emissions from combusting wood, woodchip and solid bio-fuels (by smaller-scale industrial utilities).

2.2. Amount and content of solid air pollutants

The solid material content of the flue gas was determined with different techniques during the two combustion experiments.

In the domestic-scale combustion tests, a "wet" absorption method has been used to identify solid air pollutants. The flue gas was diverted from the sampling probe into two absorption tanks filled with water. The flow volume of the flue gas circulating through the system has been measured for a present time, together with the weight of the solid residue remaining after the evaporation of the absorption fluid. The solid content of the flue gas was determined from these two values. Fly ash samples could be obtained in such small quantities that only limited options were left to determine the total heavy metal content. The average chemical composition of particulate air pollutants and of the fly ash has been determined via DX4 EDAX EDS microprobe with an AMRAY 1830 I scanning electron microscope.

During the semi-plant scale combustion experiment, we have taken fly ash samples at the sampling point located at the upper part of the chimney, where a standard sampling pipe section was installed. The amount of fly ash has been determined with gravimetric method using S-20 type cyclone probe. Isokinetic sampling has been applied during the measurement. In analysing the heavy metal content of the fly ash, all the elements were determined by ICP-AES, using a 720 ES instrument manufactured by Varian Inc., which is an axially viewed simultaneous multi-element ICP spectrometer. Calibration was done by matrix matched calibration solutions, using CertiPUR® IV multi-element ICP CRM solution by MERCK Ltd. The samples were then heated in a closed PTFE bomb in concentrated nitric acid at 130 °C for 120 minutes until complete dissolution. After cooling the bombs to room temperature, the dissolved samples were transferred into a volumetric flask, filled up to the final volume of 50 cm^3.

3. Results

3.1. The heavy metal content of biomas

As a result of the phytoremediation process, the heavy metal contaminants of the soil are accumulated in the plants. The heavy metal content of the ligneous biomass samples has been determined. The results can be seen in Table 1. Figure 3 shows the heavy metal content of the biomass samples in a diagram form.

Table 1

Heavy metal content of the combusted biomass samples (mg/kg)

Metal	**Oak**		**Poplar**	
	Domestic-scale	**Semi-plant scale**	**Domestic-scale**	**Semi-plant scale**
	mg/kg			
Zn	47.6	59.4	274	149.1
Cu	32.7	147.4	16	25.6
Cd	10.9	3.5	19	2.7
Pb	< 10	8.1	< 10	4.4
Mn	206	253.1	58	74.9
Cr	813	721	191	279.7
Ni	556	190.3	94.9	63
Co	24.8	4.3	19.1	1

The Figure 3 shows the heavy metal content of the biomass samples.

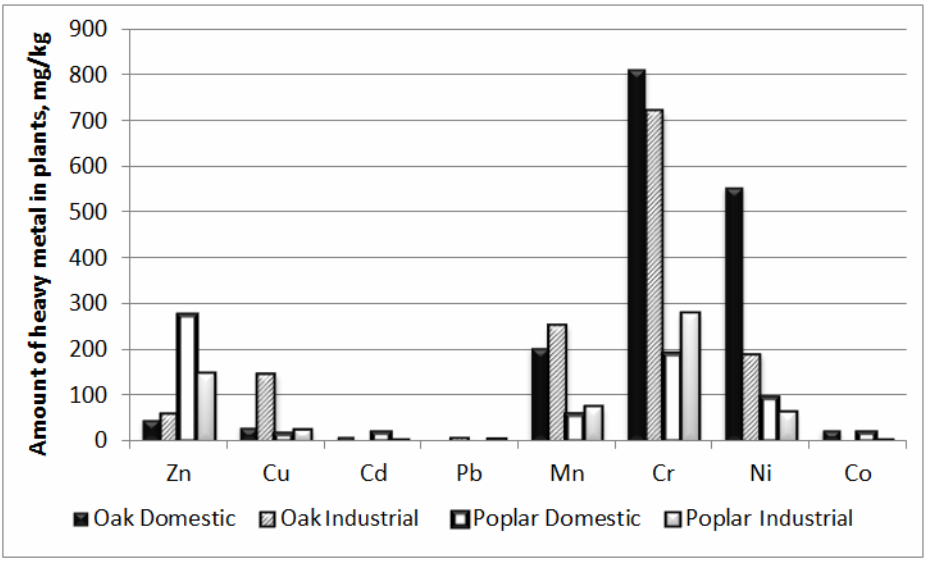

Figure 3. Heavy metal content of biomass samples

Based on the results of Table 1 it can be state that the biomass samples contain heavy metal pollutants in high amount.

3.2. Solid and gaseous pollutant emission

Specific emission values converted to the measured CO and NOx mg/m^3 values are given in Table 2 (1 ppm NOx equals to 2,05 mgNO$_2$/m^3; 1 ppm CO equals to 1,25 mgCO/m^3). Table 2 also gives information about the CO$_2$ content of the flue gas, besides its oxygen content. During the domestic-scale combustion experiment, the temperature of the flue gas at the sampling point changed between 450–500 °C, while in the semi-plant scale combustion experiment, it was between 200 and 250 °C.

The table does not contain data on the SO$_2$ content of the flue gas, since SO$_2$ emission from the fired wood samples was very low during the measurements.

Table 2

Air pollutants formed during the combustion of biomass, O_2 and CO_2 content of flue gas

Air pollutants		**Domestic-scale (7 kW)**		**Semi-plant scale (500 kW)**		**Limit value** [13]**
		Oak	**Poplar**	**Oak**	**Poplar**	
NO_x*, (11% O_2)	mg/m^3	324	156	249.02	266.74	650
CO*, (11% O_2)	mg/ m^3	268	279	177.38	***283.98***	250
O_2	% v/v	11.26	10.96	10.77	10.35	–
CO_2	% v/v	9.68	9.94	10.38	10.62	–
Solid air pollutants	mg/ m^3	25.5	165.4	***320.28***	***343.19***	150

***** *The concentrations expressed in mg/m^3 refer to flue gas with 11% oxygen content produced from dry (absolute) biomass combustion at **t** = 273 K and **p** = 101.3 kPa.*

*** Hungarian regulations give only technical limit values for the emission of air pollutants from combustion equipments with a nominal heat input capacity higher than 140 kW.*

The results are shown in Figure 4. Emission limits values are marked with a horizontal line for the semi-plant scale combustion experiment in the diagram.

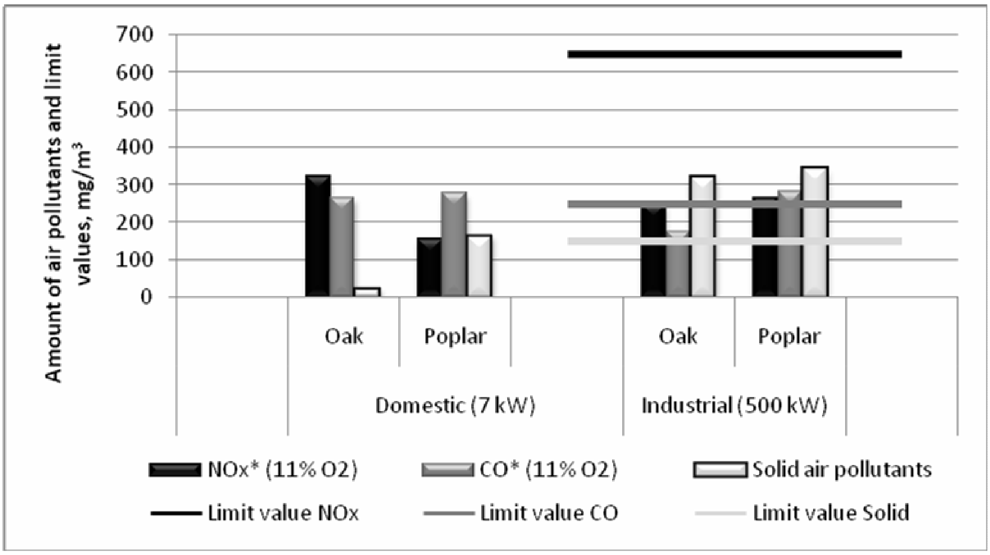

Figure 4. Amount of air pollutants formed during combustion, with limit values relevant for industrial combustion plants

As compared to the regulations currently in effect in Hungary, the measurement results of the semi-plant scale combustion experiment show that the amount of solid air pollutants formed during the combustion of wood samples is higher than the maximized limit values.

For oak samples, the emission of gaseous air pollutants remained within the limit values, while for poplar, measured CO emission exceeded the limit values by nearly 14%, with NOx emission acceptable.

4. The heavy metal content of solid air pollutants

4.1. Domestic-scale combustion experiment

In the case of the domestic-scale combustion experiment, the sampled volume of fly ash suitable for composition analysis had been so small, that we performed an electron microscopic examination instead of chemical composition analysis. The heavy metal composition of the fly ash relative to sample weight is shown in Table 3.

Table 3

Heavy metal content of the fly ash relative to fly ash weight, mg/kg

Sample	**Zn**	**Cu**	**Mn**
	mg/kg		
Oak	0.96	0.12	0.41
Poplar	2.14	0.33	0.38

Electron microscopic and energy dispersive microprobe examinations of the fly ash separated from the flue gas gave evidence of the presence of zinc, copper and manganese. Therefore, the domestic use of the examined fuels is not recommended.

4.2. Semi-plant scale combustion experiment

During the semi-plant scale combustion experiment, we have examined the heavy metal content of the fly ash taken at two sampling points. The amount of fly ash was sufficient to allow for the exact determination of its chemical composition, as presented in Table 4. Figure 5 shows the results of the examination.

Table 4

Heavy metal content of the fly ash relative to fly ash weight, mg/kg

Sample	**Zn**	**Cu**	**Cd**	**Pb**	**Mn**	**Cr**	**Ni**	**Co**
	mg/kg							
Oak	2156.6	282.6	15.1	168.3	6029.0	144.9	94.6	2.0
Poplar	3305.3	221.9	48.0	124.8	5454.1	70.6	68.7	2.9

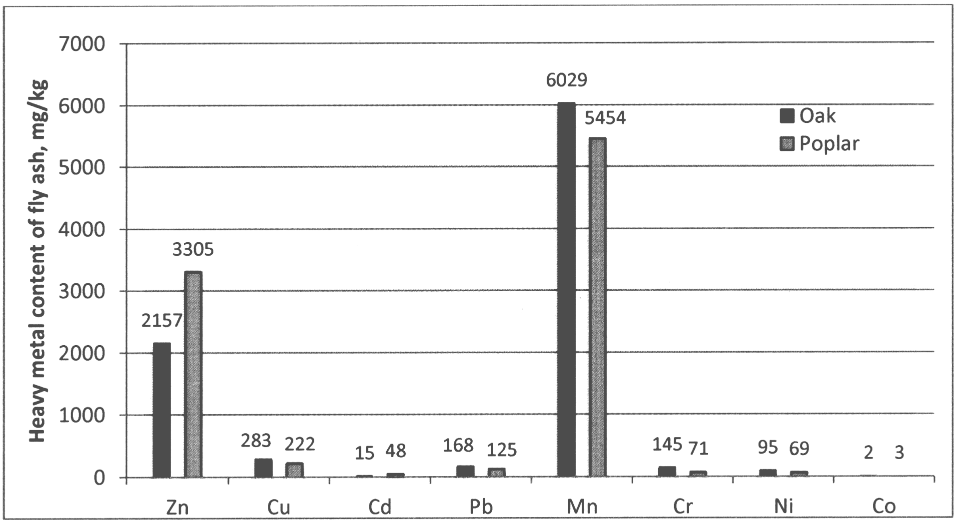

Figure 5. Heavy metal content of the fly ash samples in the case of boiler

It can be deduced from the results that – like in the case of the domestic-scale combustion experiment – the fly ash did contain all the examined metallic elements. Based on the chemical analysis, we can state that a more efficient separation of the fly ash from the flue gas is necessary in order to prevent these high heavy metal contents being released into the atmosphere. Heavy metal polluted fly ash entering the environment can cause serious environmental problems.

Conclusions

On the whole, it can be stated that in the semi-plant scale combustion experiment, the amount of gaseous air pollutants produced from the combustion of poplar samples has exceeded the emission limit values. Concerning the solid material content of the flue gas, we can say that the rate of fly ash formation is excessive for both samples. The detectable heavy metal content of the fly ash makes it necessary to improve the technological efficiency of dust collection or to replace the cyclone dust filter with a baghouse dust collection system. Based on our results, it can be determined, that the combustion device used for burning biomass grown on heavy metal polluted areas – brownfield lands – must make it possible to separate the fly ash from the flue gas and allow the proper handling of solid burning residues.

Acknowledgement

This research was carried out in the framework of the Center of Excellence of Sustainable Resource Management at the University of Miskolc.

References

[1] Jadia Chhotu, D.–Fulekar, M. H.: *Phytoremediation of heavy metals: Recent techniques*. African Journal of Biotechnology Vol. 8 (6), pp. 921–928, 2009.

[2] Barótfi I.: *Környezettechnika* (in English: Environmental Techniques). Mezőgazda Kiadó Kft., 2002.

[3] Anton A.–Murányi A.: *Hatékony fitoremediáció* (in English: Efficient phytoremediation). MOKKA Konferencia, Budapest, 2007. június, in http://enfo.hu/mokka/conference/Hungarian_Presentations/Anton_Muranyi_ppt.pdf

[4] Ogundiran, M. B.*–Osibanjo, O.: *Heavy metal concentrations in soils and accumulation in plants growing in a deserted slag dumpsite in Nigeria*. African Journal of Biotechnology Vol. 7 (17), pp. 3053–3060, 2008.

[5] Mahmood, T.–Islam, K. R.–Muhammad, S.: *Toxic effects of heavy metals on early growth and tolerance of cereal crops*. Pak. J. Bot., 39(2): 451–462, 2007.

[6] MSZ 21456/5-86 86 Examination of gaseous air pollutants. Determining carbon monoxide.

[7] MSZ 21853/19-81 Examination of air pollutant sources.

[8] MSZ 21853/6-84 Examination of air pollutant sources. Determining sulphur dioxide emission. Conductimetric, infrared, ultraviolet method.

[9] MSZ ISO 7996:1993 Ambient air. Determining the mass concentration of nitrogen oxides. Chemiluminescence method.

[10] MSZ 21453:1988 A specifications on determining solid air pollutants.

[11] MSZ 21456-37:1992 Examination of gaseous air pollutants. Sulphur dioxide.

[12] Hungarian government decree on the technological emission boundary values of air pollutants (140 kWth or -50 MWth)
in Hungarian 23/2001. (XI. 13) KöM rendelet: a 140 kWth és az ennél nagyobb, de 50 MWth-nál kisebb névleges bemenő hőteljesítményű tüzelőberendezések légszennyező anyagainak technológiai kibocsátási határértékeiről.

[13] Hungarian government decree on the technological emission boundary values of air pollutants (>50 MWth)
in Hungarian 10/2003. (VII. 11) KVVM rendelet: az 50 MWth és az annál nagyobb névleges bemenő hőteljesítményű tüzelőberendezések működési feltételeiről és légszennyező anyagainak technológiai kibocsátási határértékeiről.

Materials Science and Engineering, Volume 39, No. 1 (2014), pp. 41–50.

CHARACTERIZATION AND GD-OES INVESTIGATION OF THIN TIN ELECTROPLATED COPPER SUBSTRATES USED IN THE ELECTRONICS INDUSTRY

GÁBOR LASSÚ[1]–ÁDÁM RADÁNYI[2]–ZOLTÁN GÁCSI[3]–
TAMÁS TÖRÖK[4]

Tin electroplated copper sheets were analysed, with the aim of characterizing the structure of the thin film layer deposited on the substrate. The selected raw materials and the plating process are commonly used in the electronics industry for the manufacturing of printed circuit boards. In addition, we used a Hull cell to show the effects of current density distribution on layer deposition. Our research study involved SEM, GD-OES, and optical stereomicroscopic examinations, employed for the structural and qualitative evaluation of layer properties ("layer goodness"). It is clearly visible from the results, that bath composition is not indifferent in the electroplating process: i.e. the distinctive compounds of the bath will be detectable in the outer layers of the coating. Though at high current densities, the coating became spongy, but intermetallic transient phases (e.g. Cu_6Sn_5) were not at all observed at the Cu-Sn interface irrespective of the applied current densities. The grains so formed were mainly equiaxial, with no orientation found.

Keywords: electroplating, tin, copper substrate, Hull cell, GD-OES.

Introduction

Nowadays, a large variety of valuable metals, like tin, copper, silver, nickel, gold, etc. are present in the electronics industry. These metals are all indispensable for the manufacturing of wiring boards, electrical contacts, printed circuits boards (PCBs) and other small electronic components, that are commonly incorporated in consumer goods, e.g. mobile tools, household devices or automotives. The production technologies largely build on advanced soldering techniques like tin-base lead-free soldering, to connect solid/bulk metal surfaces (Cu, Sn, Ag, Au etc.) or metallized (i.e. metal covered) plates, with high precision. Electroplating is one of the most widely applied metal deposition methods used for creating conductive metal layers on various substrates (i.e. contact pads), e.g. pure

---

[1] University of Miskolc, Faculty of Materials Science and Engineering, Institute of Metallurgy and Foundry
3515 Miskolc-Egyetemváros, Hungary
feklassu@uni-miskolc.hu

[2] University of Miskolc, Faculty of Materials Science and Engineering, Institute of Material Science
3515 Miskolc-Egyetemváros, Hungary
femradam@uni-miskolc.hu

[3] University of Miskolc, Faculty of Materials Science and Engineering, Institute of Material Science
3515 Miskolc-Egyetemváros, Hungary
zoltan.gacsi@uni-miskolc.hu

[4] University of Miskolc, Faculty of Materials Science and Engineering, Institute of Metallurgy and Foundry
3515 Miskolc-Egyetemváros, Hungary
fektt@uni-miskolc.hu

(lead-free) thin tin layers on pure copper substrates. Of course, there are several other alternatives available for tin deposition, depending on the type of application.

A recent publication on the peculiar features of tin deposition and electrocrystallization from non-alkaline (i.e. acidic) aqueous solutions used in tin recycling processes, especially in tin electrowinning [1], and studies on the spontaneous formation of "tin whiskers" grown on pure, electroplated tin layers [2] impelled us to conduct further investigations on the structural properties of layer deposition. Thus, we performed laboratory experiments on relatively thin electroplated layers of tin deposited onto pure copper sheets, with the aim of characterizing the surface profiles. We used a methanesulfonic acid-base industrial bath obtained from a printed circuit board (PCB) manufacturer (Eurocircuits Co. Ltd. Eger). By using a Hull cell for the electroplating experiments, it was possible to follow, on a single copper cathode sheet, the effect of cathode current density distribution in a relatively wide range. All the other parameters were kept constant during the experiments.

The freshly deposited tin layers were first evaluated via visual observation. Then, several modern testing and surface analytical techniques have been applied, among them Glow Discharge Optical Emission Spectroscopy (GD OES). This method has the capacity to give an in-depth characterization of solid surface layer profiles – including the tin/copper interface and the copper substrate below – in the tens of microns range, within a few minutes measuring time.

2. Laboratory experiments

2.1. Materials and laboratory equipments

The materials used (thin copper sheets, electroplating tin bath) were obtained from the PCB manufacturer company, Eurocircuits Co. Ltd. (Eger), recognized as an online PCB prototype and small series specialist worldwide.

2.1.1. Copper sheet/foils

The thin (~90μm) copper foils (products of IMARO/ELTECH) typically had a shiny side, with an average surface roughness of R_a~ 0,2 μm, and a bonding side with a much higher R_a value. Considering these parameters, only the shiny side (Figure 1) was tin electroplated in the Hull cell, after proper cleaning and degreasing. In order to get the thin (a few nanometers thick) oxide surface layer removed, the foils underwent slight activation via short immersion in an aqueous etching solution of diluted (~ 2%) nitric acid.

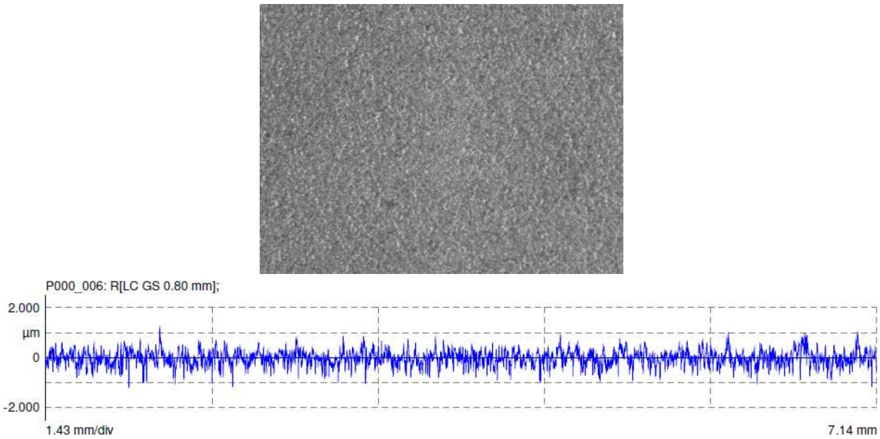

Figure 1. Photograph and profile of the shiny side of the pure copper foils used as substrates for tin electroplating (Magnification = 100 X)

2.1.2. Electroplating bath composition

For the laboratory process, we used a commercial type tin electroplating bath (RESTIN BMAT PC). This fluoroborate-free bath was originally developed for special etch-resist applications in metal etching. Today, an actual technological application of the bath by the producer Eurocircuits Co. Ltd., is SMOBC (Solder Mask Over Bare Copper), that is a preventive method designed to protect the underlying copper sheet while the unprotected thin copper layers of the PCBs are dissolved in an appropriate selective aqueous etching solution. This electroplating bath is highly acidic, due to its free methane-sulfonic-acid content varying between 120 and 200 g/dm^3. The bath contains considerable amounts of proprietary additives (so-called Primary and Secondary additives) in order to produce fine grain and smooth dense deposit. Another function of the additives is to protect the dissolved Sn^{2+} ions from oxidation to Sn^{4+} as a result of exposure to ambient air during the electrolytic process.

2.1.3. Hull cell used for tin electroplating

The Hull cell is basically a specially shaped container (Figure 2) designed originally for the practical testing of electroplating solutions. The cathode is set at a pre-defined angle to the anode (as shown in Figure 2), to produce an extensive range of current densities. The current densities produced in the Hull cell can be calculated from the geometrical data of the cell, which makes it possible to check and characterize the deposit along the cathode plate as a function of current densities – supposing that the given experiment is performed at a known constant current value (i.e. cell current is applied in the "*galvanostatic*" operation mode).

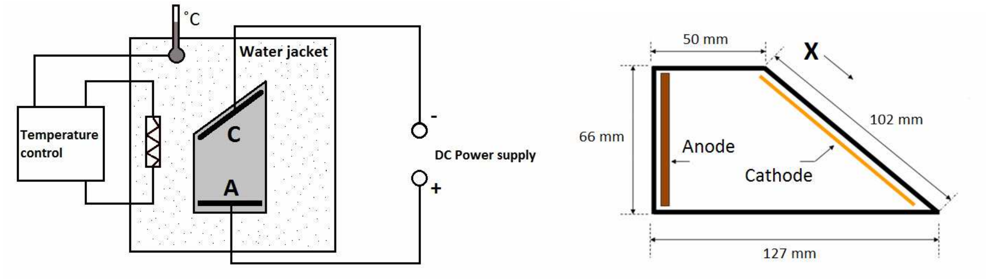

Figure 2. Schematic illustration of a home-made laboratory Hull cell (top view) placed in a water bath for temperature control. The anode plate (A) was a pure tin sheet and the cathode plate (C) was a pure copper foil, both immersed vertically in the electrolyte solution

Table 1

Characterization of the tin electroplated copper foils prepared in the Hull cell via deposition at a constant cell current of 1 A at 30 °C.

Sample No.	**Position on the cathode plate, *X*** (mm)	**Calculated cathode current density, *j*** (A/dm^2)	**Appearance of the tin deposit**
Sample 1	*84*	*0.26*	*Light silvery grey*
Sample 2	*73*	*0.58*	*Light silvery grey*
Sample 3	*68*	*0.74*	*Shiny silvery*
Sample 4	*60*	*1.02*	*Shiny silvery*
Sample 5	*59*	*1.06*	*Smooth grey*
Sample 6	*50*	*1.44*	*Smooth grey*
Sample 7	*49,5*	*1.46*	*Smooth grey*
Sample 8	*45*	*1.68*	*Smooth grey*
Sample 9	*43*	*1.78*	*Smooth grey*
Sample 10	*35*	*2.25*	*Smooth grey*
Sample 11	*33*	*2.38*	*Dull grey*
Sample 12	*25*	*3.01*	*Dull grayish black*
Sample 13	*17*	*3.89*	*Microgranulous dull grey-black*
Sample 14	*7*	*5.91*	*Microgranulous dull blackish*

Cathode size:	100 mm x 75 mm
Anode size:	75 mm x 50 mm x 7.5 mm
Solution volume:	267 ml

Current distribution is based upon the formula:

$$-j=I(5,1-5,24\cdot\lg X),$$

where

j = current density (A/dm^2)

I = total current (A)

X = distance from the high current density end of the panel (mm)

2.2. Instrumentation

2.2.1. Optical stereomicroscopy

Stereomicroscopes are variants of optical microscopes, designed for qualitative depth profiling. These devices allow the observation of sample images with high spatial resolution, typically using light reflected from the surface of an object, rather than transmitted through it. This imaging method provides a three-dimensional visualization of solid samples even with complex surface topography, where the three-dimensional view offers special advantages for the detailed analysis of the surface profiles. For this purpose, we used a Zeiss Discovery V12 Stereo Microscope. The SteREO Discovery series incorporates three options, with zoom factors of 8, 12 and 20; whereby the V12 set offers a motorized 12:1 zoom, with excellent depth resolution.

2.2.2. Scanning electronmicroscopy

The morphology of the samples was investigated by using a Zeiss EVO MA type Scanning Electron Microscope, equipped with an EDAX Genesis APEX 2 system for energy-dispersive X-ray microanalysis. Microphotographs of 1000x magnification were obtained with BSE ("back scattered electrons") method. This technique allowed the precise mapping not only of sample topography, but of compositional contrasts as well.

2.2.3. Glow Discharge Optical Emission Spectroscopy (GD OES) with Depth Profiling

Thin film analysis with various sputter-depth-profiling techniques is based on the erosion of material surfaces as a result of energetic particle bombardment (mostly ion bombardment), whereby the material (i.e. the constituting atoms) is being removed continuously as a function of sputtering time. These analytical techniques can be divided in two main groups: "removed-matter" techniques and "remaining-surface" techniques. In the "remaining-surface" type analytical techniques (e.g. XPS – photoelectron spectroscopy, AES – Auger electron spectroscopy), the surface obtained by sputtering is analysed; while in the "removed-matter" techniques (e.g. secondary ion mass spectrometry – SIMS, laser ablation inductively coupled plasma mass spectrometry – LA ICP MS, glow discharge optical emission spectrometry – GD OES and glow discharge mass spectrometry – GD MS), the analysis of the sputtered material as a function of sputtering time allows the determination of the compositional distribution of a thin film (formed from the extracted material on a suitable substrate) against the distance from the original (sample) surface [3].

In our case, the GD OES analysis was performed with a GD-Profiler2 instrument manufactured by HORIBA Jobin Yvon (Longjumeau, France). This instrument is equipped with a radiofrequency generator (operating at 13.56 MHz frequency) and a standard HJY glow-discharge source with an internal anode diameter of 4 mm, which corresponds to the exact surface area detected on the tin coated copper foil samples in each GD OES investigation process (as listed in Table 1). GD operation mode with "*constant pressure-constant forward power*" setting (450 Pa pressure, 40 W ***rf***-forward power) was used for each experimental series. After the proper mode of operation had been set – i.e. the discharge and sputtering conditions were determined in a way to optimize the crater shape – the glow discharge process was initiated. The measured experimental curves of the light intensities emitted by the respective elements (i.e. the elements present in the sampled tin deposit to the depth of the copper substrate) were being recorded (Figure 3).

A crater with tin islands

A crater down into the Cu substrate

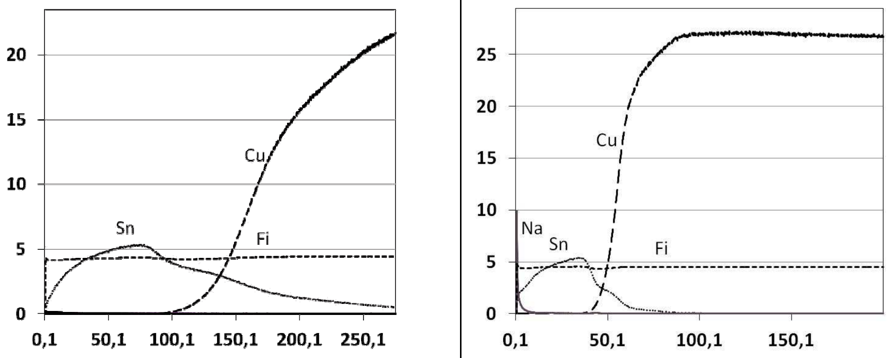

The registered spectrum of sample 14

The registered spectrum of sample 3

Figure 3. Above: Stereoscopic images (N = 50x) of the craters formed by glow discharge (GD) argon sputtering during the GD OES depth profile analysis of tin electroplated samples deposited on copper foils/substrates. Below: spectrums indicating the light intensities of emitted photons (vertical axis) as a function of sputtering time (horizontal axis)

3. Results and discussion

The studied tin electroplated copper sample sheets (measured total surface area: ~ 100mm x 75 mm), were characterized by light greyish smooth surface, except for the region where deposition was taking place at the highest current densities (See Table 1). In this region, the tin deposit was blackish dull and grainy. The GD OES depth profile analysis was performed along the longer edge of the samples, in the middle region towards the grainy zone. Starting from the side with lower current densities, 14 GD sputtering experiments were performed on each tin electroplated specimen, in about 1 cm steps between the craters formed. Three representative set of steps are shown in Figure 4, with the results obtained from the GD OES experiments.

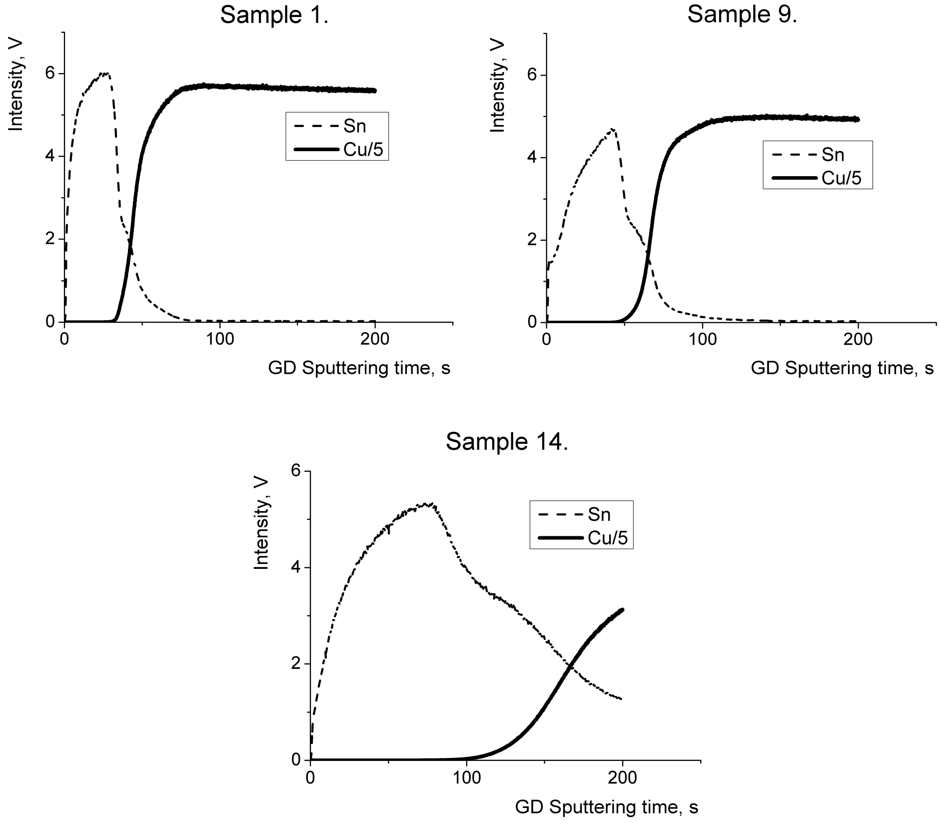

Figure 4. GD OES depth profile analysis. Spectra recorded for the respective samples at increasing current densities and uniform sputtering time intervals for each GD sputtering experiment

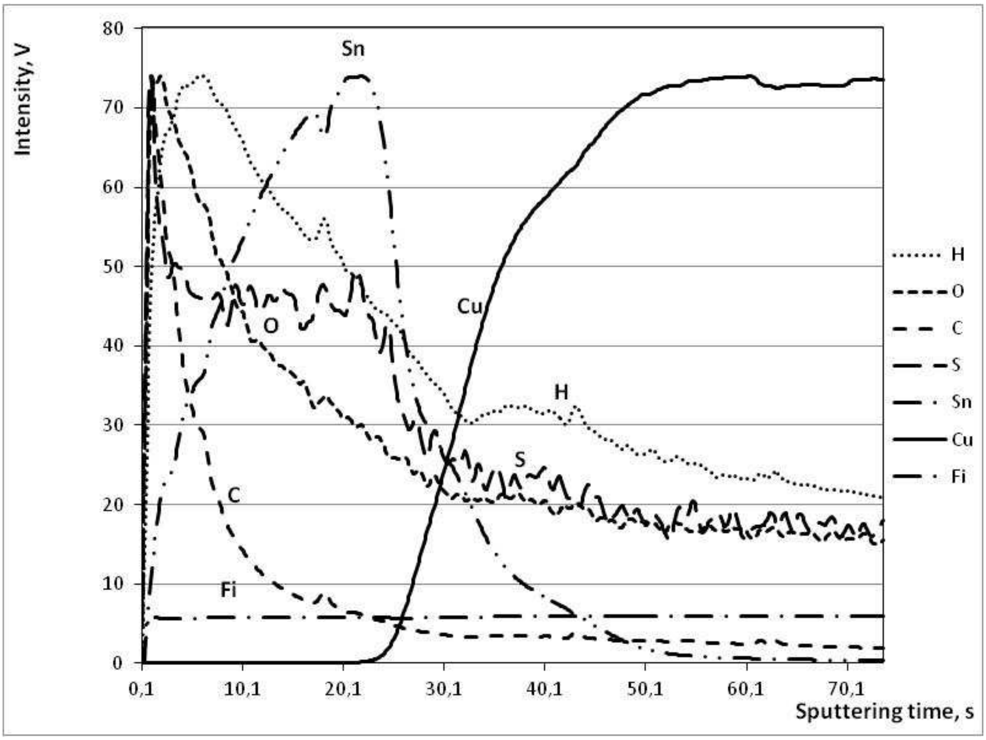

Figure 5. GD OES signal intensities maximized (except for copper) to show the constituting elements (Sn, C, O, H and S) of the tin electroplating bath slightly incorporated in the thin tin deposit.

As it is apparent from Figure 5, the outermost surface of the tin plated sample was supposedly exposed to slight oxidation in air and got slightly contaminated with some carbon containing material (e.g. finger print). Internally, the presence of evenly distributed sulfur is also recognizable.

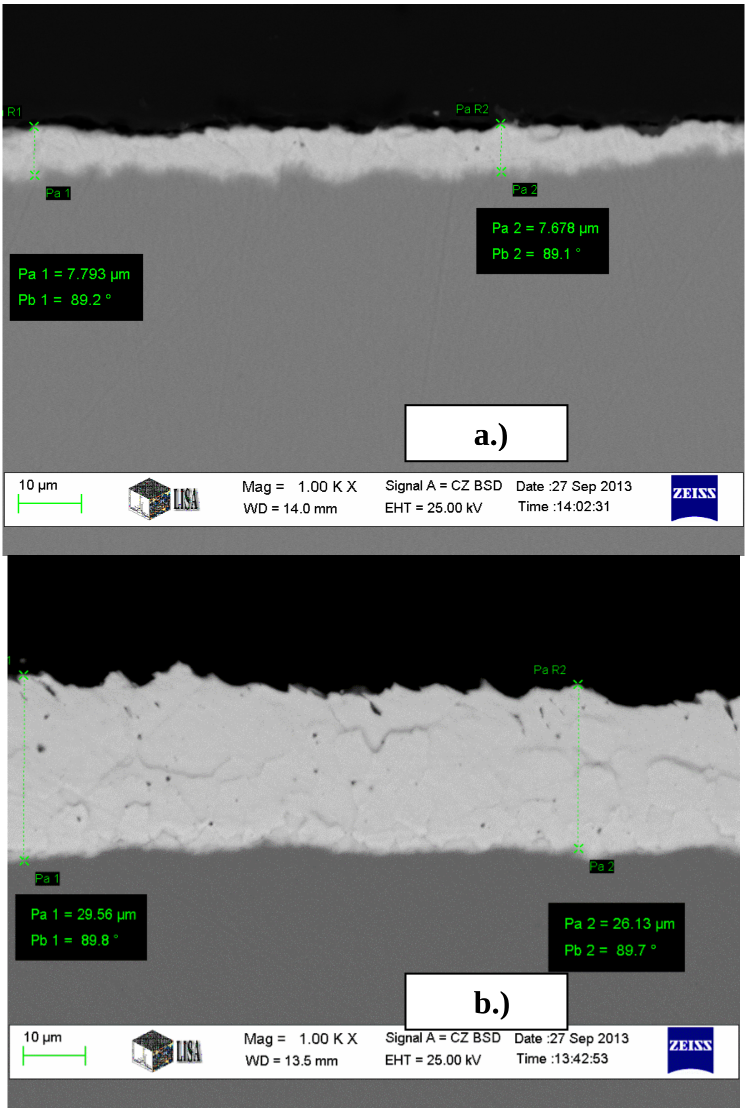

Figure 6. a–b) Cross section SEM images of two tin electroplated samples: a) thin tin layer; b) thick tin layer

In Figure 6, the grain structure of the deposits is seen to be quite fine and equiaxed, not columnar. Though, at some regions a few small voids can be observed. These can be attributed to a certain extent of hydrogen co-deposition accompanying the cathodic reduction of tin. With the occasional mixing of the plating solution or the vibration of the cathode plate, the presence of hydrogen could most probably have been reduced. However, in a small Hull cell like ours, such mechanical modifications were not possible to implement. Based on the observed microstructure of the thin tin layer, no risk of whiskers formation is expected – as it follows from recent reports on the explanatory results of spontaneous whiskers growth [2]. Moreover, the thin tin layer deposited from the given industrial methane-sulfonic-acid type tin plating bath did not show any proneness to Cu-Sn intermetallic compound formation. Of course, the probability of Sn-Cu intermetallics formation cannot be excluded if, for example, the deposited layer produced at ambient (~30°) temperature would be exposed to higher temperatures for longer periods of time.

Summary

In this paper, we presented some details of the coating structures, and the effects of current density distribution on structure formation of thin tin layers formed on pure copper sheets during our laboratory electroplating experiments. At higher (i.e. > 2.5 A/dm^2) current densities the thin tin deposits were darker greyish and more microgranulous (slightly spongy). However, the tin deposits microstructure were always (at least within the studied current range of about 0.3–4 A/dm^2) quite fine and equiaxed, not columnar. Right after deposition no sign of Sn-Cu intermetallics formation could be observed. Nevertheless, slight incorporation of sulphur was detected by the GD OES depth profile measurements in the deposits so obtained from the given and highly acidic methane sulfonic acid tin industrial electroplating bath.

Acknowledgements

The described work was carried out as part of the TÁMOP-4.2.2.A-11/1/KONV-2012-0019 project in the framework of the New Széchenyi Plan. The realization of this project is supported by the European Union, co-financed by the European Social Fund.

Special thanks to Tibor Kulcsár for his help in executing the GD OES measurements as well as to Ms Viktória Molnár (Eurocircuits Co.Ltd. Eger) for supplying the materials for the experiments.

References

[1 Rimaszéki, G.–Kulcsár, T.–Kékesi, T.: *Application of HCl solution for recovery the high purity metal from tin scrap by electrorefining*. Hydrometallurgy 125–126 (2012) 55–63.

[2] Miller, S. M.–Sahaym, U.–Norton, M. G.: *Effect of substrate composition on Sn whisker growth in pure Sn films.* Metallurgical and Materials Transactions A, 41A (2010) 3386–3395

[3] Pisonero, J.–Fernandez, B.–Pereiro, R.–Bordel, N.–Sanz-Medel, A.: *Glow-discharge spectrometry for direct analysis of thin and ultra-thin solid films.* Trends Anal. Chem. 25 (2006) 11–18.

Materials Science and Engineering, Volume 39, No. 1 (2014), pp. 51–57.

STUDY ON THE ELECTROLYTIC DEGRADATION OF SULPHIDE-CONTAINING CHEMICAL RESIDUES FROM WASTEWATER IN SALINE SOLUTION

FERENC MOGYORÓDY[1]

The anodic oxidation of organics is a potentially effective technique to control pollutant contents in industrial and communal wastewaters. The electrolytic degradation of sulphide-containing chemical residues was studied using Pt and DSA® (RuO_x plated Ti) electrodes in saline solution. The applied method was highly effective, as shown by HPLC measurements.

Keywords: anodic oxidation, DSA®-electrode.

Introduction

The treatment of chemical residues in communal wastewater is a serious and so far unresolved problem. Electrochemical techniques are often considered as a viable solution for the elimination of toxic compounds contained in certain effluents and wastewaters [1]. Many industrial effluents are formed from wastewater-containing organic pollutants, which must be mineralised via/through oxidation in CO_2, H_2O, Cl^-, SO_4^{2-}, NO_3^- *etc.*

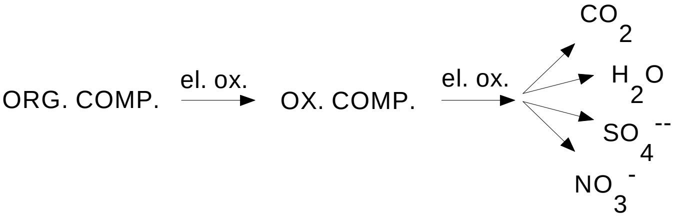

Of all the organic pollutants, the most toxic are chlorinated and aromatic solvents, pesticide and chemical warfare agent residues *etc*. It is now an established fact/Researchers agree on the fact, that a simple modification in the molecular structure can considerably reduce the toxicity of a compound [2]. Electrochemistry, therefore has its part to play in providing pre-treatment technologies to destroy refractory pollutants that bacteria have great difficulty in digesting during the process of biological degradation. The anodic oxidation of sulphide-containing chemical residues such as dimethyl-sulphide (DMS) and 2,2'-dihydroxyethyl-sulphide (DHES, thiodiethanol) were studied in this work.

---

[1] University of Miskolc, Institute of Chemistry,
3515 Miskolc-Egyetemváros, Hungary
fkmmf@.uni-miskolc.hu

1. Experimental research/Laboratory experiments

For the anodic oxidation of the model compounds, a three-electrode system with unseparated electrode chambers connected to a potentiostate was used (Figure 1). A potentiostate with Ag/AgCl reference electrode and a double recorder output (capable of producing 0–10 A current at 0–4 V constant voltage stabilised with an accuracy of ±0.01 V) was applied as power supply.

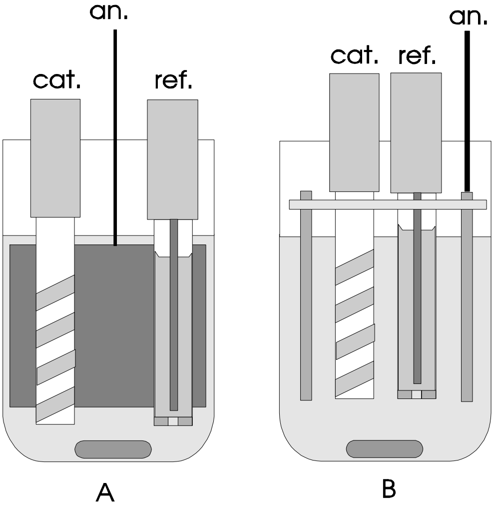

Figure 1. Schematic diagram of the electrolysis cells.
Cell A: platinum anode, platinum cathode, Ag/AgCl reference
Cell B: DSA® anode, platinum cathode, Ag/AgCl reference
Both cells were vigorously stirred during electrolysis

Constant potential was maintained by an EF 427 type potentiostate. The intermediates produced were analysed by a Hewlett-Packard 1084B HPLC. A Hewlett-Packard 8452A diode-array spectrophotometer was also applied.

Dimethyl-sulphide was freshly distilled from sodium metal directly before use, and stored under dry and oxygen-free nitrogen atmosphere using Schlenk-type glassware. Thiodiethanol was purchased and stored under dry nitrogen atmosphere and used without further purification. Stock solutions of 0.5 M for sodium-chloride, and 1000 ppm and 200 ppm for DMS and DHES, were used respectively.

2. Results and Discussion

In order to facilitate pollutant/contaminant oxidation with hypochlorite, we tried to form *in situ* hypochlorite via electrolysis. The production of hypochlorite by electrolysis has already been examined from several aspects, as reported in the (available) literature. Kelsall *et al.* [3] studied the electrolysis of NaCl in aqueous solution.

In the absence of an oxidizable organic molecule, the two basic electrode reactions in sodium-chloride solution are the following:

$$\text{Anode:}\quad Cl^- + 2\,OH^- = OCl^- + H_2O + 2\,e^- \qquad (1)$$

$$\text{Cathode:}\quad 2\,H_2O + 2\,e^- = H_2 + 2\,OH^- \qquad (2)$$

Electro-oxidation of DMS. The presence of an organic sulphide may significantly change the anode reaction. Depending on the electrode potential and the material of the anode, two different mechanisms can be proposed. The indirect anodic oxidation of dimethyl-sulphide (DMS) with *in situ*-generated hypochlorite ions results in dimethyl-sulphoxide (DMSO) and dimethyl-sulphone (DMSN) consecutively (Scheme 1).

Scheme 1
Indirect anodic oxidation of DMS with *in situ*-generated hypochlorite:

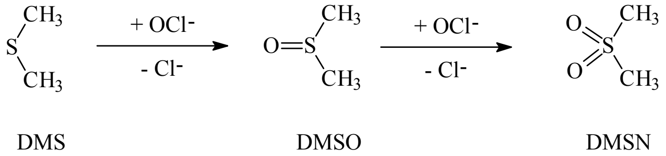

The direct anodic oxidation of DMS on platinum gave exclusively DMSO in 30 minutes. At the end of the process, no hypochlorite was found in the solution by UV spectroscopy. A continuous loss in current intensity was also observed, which finally led to the interruption of the electrolytical process. Using reversed phase HPLC technique for the monitoring and identification of the products formed in the reaction, DMSO was the only detectable product. Normalised integral values of the peak concentrations of the components are shown in Figure 2 as a function of time.

Reversed potential applied on the platinum wire mesh for 30 seconds gave a significant current jump, indicating that the surface of the electrode might have become partially blocked by the end of the electrolytical process.

In order to observe/examine the effect of the anode material on the quality of the products, we repeated the experiments using a DSA anode, which was supposedly less sensitive to sulphur-containing substances than platinum. (Sulphur is catalysator poison.) Normalised integral values of the peak concentrations of the components are shown in Figure 3 as a function of time.

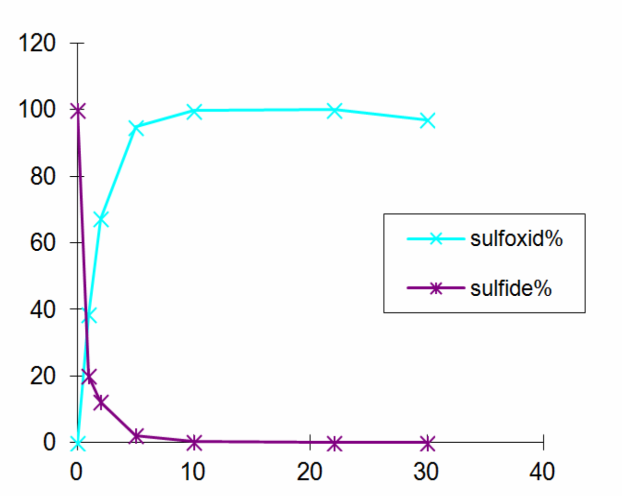

Figure 2. Normalised integrals of the peak concentration values of DMS and DMSO in an electrolysis experiment carried out using an anode made of platinum mesh, plotted against time. The electrode potential (relative to Ag/AgCl electrode) was 1.35 V. Current intensity dropped from 200 mA to 9 mA during the experiment

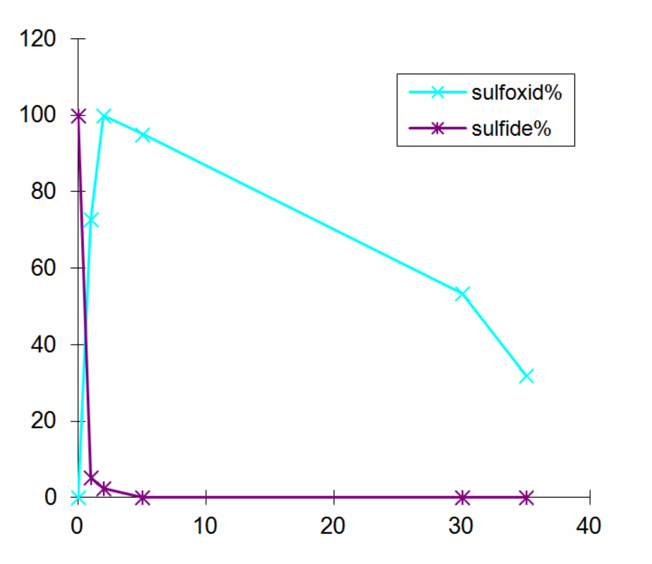

Figure 3. Normalised integrals of the peak concentration values of DMS and DMSO in an electrolysis experiment carried out using DSA$^{®}$, plotted against time. The electrode potential (relative to the Ag/AgCl electrode) was 1.35 V

As seen in Figure 3, DMSO formed in the first step produced/gave a maximum curve indicating that further reactions are expected to follow. However, due to the interference of the increasing amount of hypochlorite ions, no DMSN was identified with HPLC/UV absorbance.

Since no hypochlorite was formed at 1.35V on the platinum cathode, yet the electrode reaction did take place, it is very likely that the mechanism is different from a simple chemical oxidation by hypochlorite. We suggest that in the described case, a direct anodic oxidation of DMS to DMSO takes place (see Scheme 2, Step 1), which might be followed by a second direct oxidation step on the DSA$^{®}$ anode (Scheme 2, Step 2), with a simultaneous formation of hypochlorite ions triggering the indirect oxidation of DMSO [5].

Scheme 2
Direct anodic oxidation of DMS:

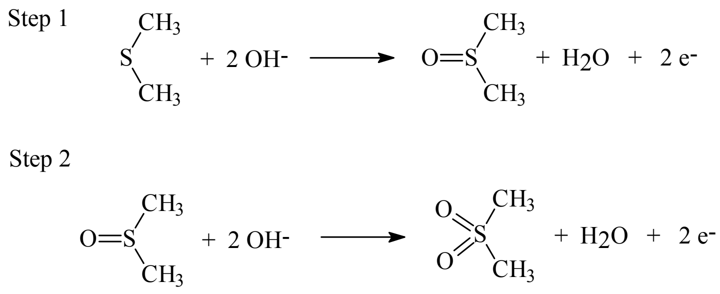

Electrooxidation of DHES. On the basis of the experiments performed with DMS, further studies with the non-toxic hydrolytic product of HD, 2,2'-dihydroxyethyl-sulphide (DHES, thiodiethanol), have been carried out.

In strongly alkaline aqueous solutions, DHES is formed from HD at a moderate to good rate, as described by/explicated by Scheme 3.

Scheme 3
Simple basic hydrolysis of HD to dihydroxyethyl sulfide (DHE

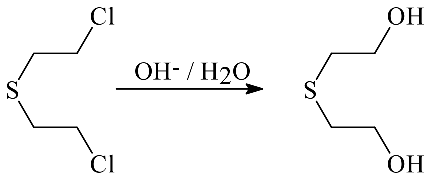

HD DHES

The smoothly proceeding electrolytic oxidation of DHES on DSA$^{®}$ anode results in two major products, DHESO and DHESN, as shown in Figure 4 and Scheme 4.

Scheme 4
Anodic oxydation of DHES

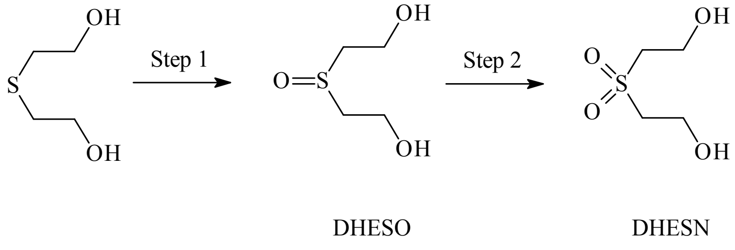

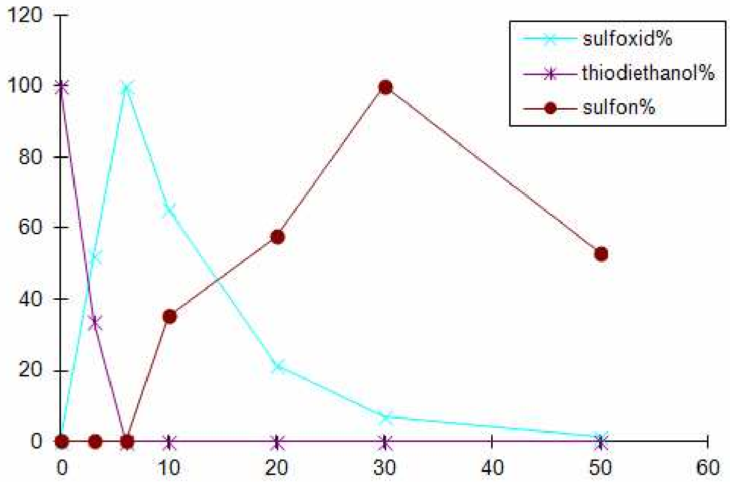

Figure 4. Normalised integral values of the peak concentrations of DHES, DHESO and DHESN in an electrolysis experiment carried out using DSA® anode, plotted against time. The electrode potential (relative to the Ag/AgCl electrode) was 1.35 V

At high electrode potentials (2 V/0.5 A), the final decay in electrolyte performance induces further reactions of the DHESN derivatives, either with the strong base present in the electrolyte or in the form of an anodic oxidation process, which produces two major and so far unidentified products. Judging by their very high molar absorbances and HPLC peak parameters, these substances might as well be unsaturated macrocycles or linear unsaturated polymers formed from unsaturated vinyl-derivatives and/or the recombination of free radicals produced in a direct anodic oxidation step, but the full characterisation of these components requires further research.

Conclusion

Based on our measurements, it can be concluded that the sulphide-containing chemical residues can be decomposed by electrolysis, which may be applied as a new method for communal wastewater treatment, because the electrolytic treatment represents lowest environmental hazard, works rapidly and well in very dilute solutions at the ppm level and can be make automatic in a continuous technology.

Acknowledgement

The described work was carried out as part of the TÁMOP-4.2.1.B-10/2/KONV-2010-0001 project in the framework of the New Hungarian Development Plan. The realization of this project is supported by the European Union, co-financed by the European Social Fund.

References

[1] Kreysa, G.– K. Jüttner, K.: 3. ESEE. Nancy, 1994, p. 247.
[2] Seignez, S.–Pulgarin, C.–Péringer, P.–Comninellis, C.–Plattner, E.: *Swiss. Chem.* 1992, 14, 25.
[3] Boxal, C.–Kelsall, G. H.: *ICHEME SYMPOSIUM,* No. 127. p. 59.
[4] Vidal, A.–Dinya, Z.–Mogyoródy, F.: Applied Catalysis. B: Environmental 21 (4) (1999) 259–267.
[5] Mogyoródy, F.: J. of Appl. Electrochemistry, 36 (7) (2006) 765–771.

Materials Science and Engineering, Volume 39, No. 1 (2014), pp. 59–67.

DETERMINATION OF THE GAS PERMEABILITY OF HYDRAULIC BONDED REFRACTORY CONCRETE

ISTVÁN SZŰCS[1]–TAMÁS KOÓS[2]–JÁNOS TÓTH[3]

During the solidification process of alumina and zirconia electrocast refractories – used for glass melting furnaces – dangerously sharp crystals can occur inside the shrinkage cavity. For the safe insertion of the blocks into the melting furnace, the shrinkage cavity must be sealed with refractory concrete.

The aim of our research was to determine the most important characteristics of refractory concrete: the mass and heat changes that take place during the first heat-up and gas permeability. Special laboratory measurements were carried out in order to determine the temperature and gauge pressure values in the shrinkage cavity sealed with refractory concrete during the first heat-up of the refractory block. The measurement data shows, that with 100 °C or above in the cavity (the boiling temperature of the water), the maximum overpressure was around 1300 Pascal. We can declare, that the gas permeability of the sealing refractory concrete allows the steam to leave released from the cavity at safe, low gauge pressure levels.

Keywords: electrocast refractories, solidification cavity, refractory concrete, gas permeability.

Introduction

In the solidification process of alumina and zirconia electrocast refractories melted in electric arc furnace, close to the point when the melted material is casted into the mould, dangerously sharp crystals would occur in the shrinkage cavity formed by the casting. For the safe building-in of the block into the glass melting furnace, this solidification hole must be covered with hydraulic bonded refractory concrete [1].

The aim of our research was to determine the most important parameters and conditions for the safe application of refractory concrete used for sealing of the solidification hole:

- the mass and heat changes occurring during the first heat-up;
- the gas permeability of the refractory concrete;
- the temperature measured in the shrinkage cavity;
- the gas pressure prevailing in the solidification hole covered with refractory concrete during the first heat-up of the refractory block.

The following types of refractories were examined:

- electrofused Aluminate-Zirconia-Silicate refractory block (AZS: $Al2O_3 = 66\%$, $ZrO_2 = 21\%$, $SiO_2 = 12\%$, $Na_2O+Fe_2O_3 = 0,4\%$) [2, 3];

---

[1] University of Miskolc, Department of Combustion Technology and Thermal Energy
3515 Miskolc-Egyetemváros, Hungary
tuzsi@uni-miskolc.hu
[2] University of Miskolc, Department of Combustion Technology and Thermal Energy
3515 Miskolc-Egyetemváros, Hungary
tuzkt@uni-miskolc.hu
[3] University of Miskolc, Research Institute of Applied Earth Science
3515 Miskolc-Egyetemváros, Hungary
toth@akki.hu

- hydraulic bonded refractory concrete made from cement Almatis CA 25-R, (Al_2O_3 = 81%, CaO = 18%, SiO_2 = 12%, Na_2O = 0,6%, Fe_2O_3+MgO = 0,6%), made with 16 m/m% of water) [4].

1. Mass changes and thermal processes during the first heat-up of the refractory concrete

1.1. Measurement method for the determination of mass change and thermal processes

While heating refractory cement Almatis CA 25-R (prepared with 16 m/m% of water) after two days of hardening and drying, the mass change of the material and different thermal processes have been determined using a "DERIVATOGRAPH-C" type instrument applicable for computing thermal analysis [5]. Three curves were produced from the test results:

- Thermogravimetry (TG, %), indicating mass change;
- Differential-thermogravimetry (DTG, %/°C), indicating the derivative of mass change;
- Differential-thermal analysis (DTA, °C), a curve of endothermal and exothermal thermal processes.

The derivatogram registered by the instrument during the measurement is shown in Figure 1. the results obtained by evaluating the derivatogram can be seen in Table 1.

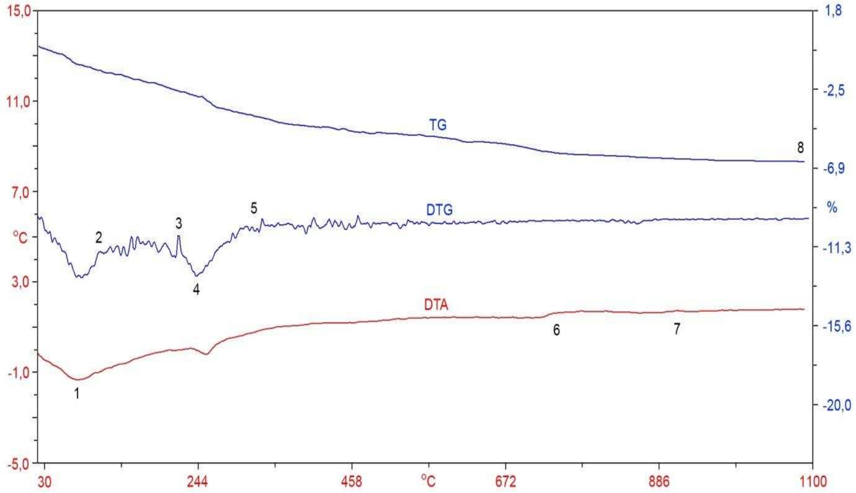

Figure 1. Derivatogram of cement Almatis CA 25-R (after two days hardening and drying). Mass change and heat processes during first heating depend on temperature

Table 1

Relevant values of the derivatogram belonging to sample Almatis CA 25-R cement

Index in *Fig. 1.*	**T, °C**	**TG, %**	**DTA, °C**	**DTG, mg/min**
1	95	–0,61	–1,261	–0,4
2	145	–2,05	–0,631	–0,213
3	215	–2,5	–0,361	–0,29
4	230	–3,22	–0,011	–0,169
5	315	–4,08	–0,053	–0,126
6	735	–6,03	1,601	–0,069
7	910	–6,39	1,732	–0,005
8	1100	–6,41	1,807	–0,028

1.2. Summary of the thermo-analytical test results of the refractory concrete

Based on data of Table 1, we can say the following:

- The mechanical water mixed into the sample to adjust its plasticity continues to evaporate up until 120–125 °C.
- The most intensive water release occurs at the narrow temperature range of 95–105 °C. The rate of evaporation gradually decreases above 110 °C.
- At the temperature range of 215–315 °C, a second phase of water release can be registered.
- The dehydration process of the AH_3 bond is the most intensive around 230 °C.
- The degradation of the Ca_3AlH_6 bond terminates at 315–320 °C.
- The total mass loss of the refractory concrete at 320 °C is 5% on average.
- At temperatures above 320 °C, the very slow-rate degradation of more complex $C_kA_mH_n$ bonds occur in multiple steps, accompanied by steady mass loss [6].
- Mass loss processes end at 910 °C, with a total mass loss of 6,41 %.

2. Measuring the gas permeability of the refractory concrete

2.1. Gas permeability measurement method

The rate of water evaporation from the refractory concrete in the shrinkage cavity during the first heat-up strongly depends on the gas permeability of the concrete. The method and the instrument of measurement tests were provided by the Department of Reservoir Engineering of the University of Miskolc.

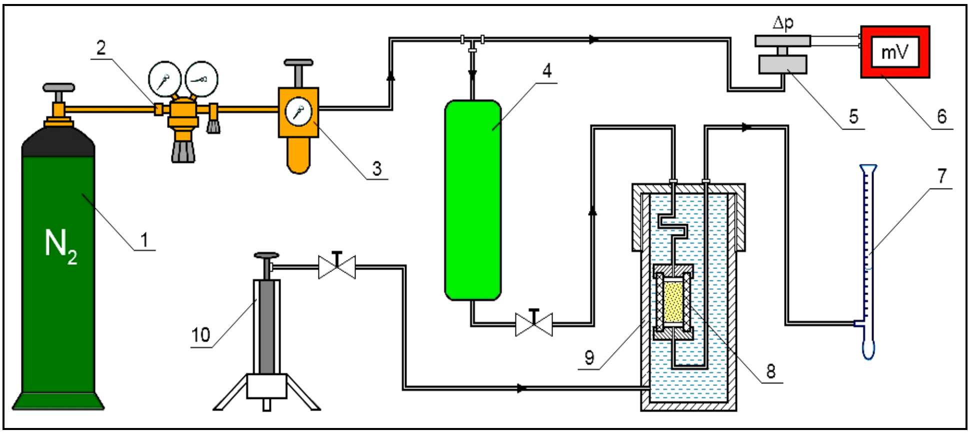

Figure 2. Measurement setup for the gas permeability test.
1 – nitrogen tank, 2 – gas reducer, 3 – fine adjustment gas reducer, 4 – puffer tank, 5 – Δp pressure transducer, 6 – voltmeter, 7 – flow meter, 8 – test sample in the HASSLER sleeve, 9 – pressure resistant container filled with water, 10 – pump to increase water pressure

Gas flow volume rate was calculated from the measured data in cm^3/sec units. From the measured values, the air and gas permeability values of the sample were determined for every increment of ***Δp*** pressure change, using EXCEL software. The modified Darcy equation was used for the calculations:

$$k_g = \frac{q_{ga} p_a \mu_g L}{A} \cdot \frac{2}{p_1^2 - p_a^2} \cdot \frac{1000}{0.9869} \qquad [\text{mD}] \tag{1}$$

where:

k_g – permeability of the sample at a given pressure difference, (milliDarcy), mD;
A – cross section of the sample perpendicular to the gas flow, cm^2;
L – sample length, cm;
p_a – exit pressure of the gas flow (normal atmospheric pressure), bar;
q_{ga} – measured flow volume rate of the gas at the exit pressure, cm^3/s;
μ_g – the viscosity of nitrogen gas, at average test pressure and temperature, cP, or mPa.s;
p_1 – entry pressure of the gas, bar.

The pressure values registered in *bars* by the pressure transducer can be converted to *atm* by using a factor of 1000/0,9869, which allows to get the respective gas permeability values in the above formula in units of *mD*.

Equation (2) seen below was formulated by plotting each ***k_g*** value of gas permeability (registered at Δ***p*** pressure differences) against the reciprocal value of average test pressure (***$1/p_{av}$***) and by using the least squares method to fit a straight line onto the points. With this formula, the absolute (Klinkenberg) permeability of the sample and the constants (**k_{abs}, b**) of the Klinkenberg formula characterizing the gas permeability of the test sample can be determined:

$$k_g = k_{abs}\left(1+\frac{b}{p_{av}}\right) = k_{abs} + k_{abs} b \frac{1}{p_{av}} = k_{abs} + m\frac{1}{p_{av}} \tag{2}$$

where

k_{abs} – absolute (Klinkenberg) permeability, mD;
b – Klinkenberg constant, bar;
k_g – measured gas and air permeability, mD;
p_{av} – average pressure of the measurement $(p_1+p_a)/2$, bar.

Equation (2) defines a straight line, the axis crossing point of which is the absolute permeability of the sample (k_{abs}), while the ***b*** parameter of the Klinkenberg formula can be determined from its gradient:

$$b = \frac{m}{k_{abs}} \tag{3}$$

where

m – the gradient of the straight line (directional tangent), mD/bar.

In some cases, Darcy's law used to formulate the Klinkenberg formula *(2)* cannot be applied to describe the gas flow through the core samples. This occurs when gas flow velocity is too high and the flow behaviour of the gas changes from linear to turbulent. In such cases, average gas permeability can be determined by a more universal mathematical formula that applies to the full pressure range of the measurement.

The determination of average gas permeability should be based on the Forchheimer formula, a widely accepted equation describing turbulent gas flows:

$$-\frac{dp}{dl} = av + bv^2 \tag{4}$$

where **a** and **b** are constants, and $v = q/A$ is the leakage rate of the gas. Cornell and Katz replaced the constants in *Equation (4)* by the following physical parameters:

$$-\frac{dp}{dl} = \left(\frac{\mu}{k}\right)v + \beta\rho v^2 \tag{5}$$

where

μ – gas viscosity, mPa.s;
σ – gas density, g/cm^3;
k – permeability of the porous core, mD;
β – coefficient for high velocity gas flow.

β coefficent in *Equation (5)* is the parameter of the core sample that makes it possible to apply Darcy's law:

$$-\frac{dp}{dl} = \left(\frac{\mu}{k}\right)\frac{q}{A} + \beta\rho\left(\frac{q}{A}\right)^2 \tag{6}$$

Assuming that the flow is isometric during the test and the nitrogen gas used under laboratory conditions is an ideal gas, gas density can be determined by the following formula:

$$\rho = \frac{Mp}{RT_a} \tag{7}$$

Substituting the appropriate density values in *Equation (5)* and performing the integration considering the limits x = 0, $p = p_1$ $p = p_a$, we get:

$$p_1^2 - p_a^2 = \left(\frac{2\mu L}{k}\frac{p_a}{A}\right)q_g + \left(\beta\frac{2LMp_a^2}{A^2RT_a}\right)q_g^2 \tag{8}$$

Equation (8) is practically identical with the one applied to linear gas flow in porous media:

$$p_1^2 - p_a^2 = A_0q_g + B_0q_g^2 \tag{9}$$

Comparing *Equations (8)* and *(9)*, it can be deduced that the constant $\mathbf{A_0}$ in E*quation (9)* can also be defined by the formula below:

$$A_0 = \left(\frac{2\mu L}{k}\frac{p_a}{A}\right) \tag{10}$$

$$B_0 = \left(\beta\frac{2LMp_a^2}{A^2RT_a}\right) \tag{11}$$

The constants $\mathbf{A_0}$ and $\mathbf{B_0}$ can be determined with the least squares method. Average gas permeability for the porous matter can be determined from point $\mathbf{A_0}$ of the straight line fitted onto the measurement points crossing the axis:

$$k_{g,avg} = \left(\frac{2\mu L}{A_0}\frac{p_a}{A}\right) \tag{12}$$

Using the appropriate values in the formula, we get the following equation for the determination of average gas permeability:

$$k_{g,avg} = \left(\frac{2000\cdot\mu_g\, L\cdot 0.9869\, p_a}{A_0A}\right) \tag{13}$$

The average gas permeability $\boldsymbol{k_{g,avg}}$ of the sample can be calculated by determining the constants $\mathbf{A_0}$ and $\mathbf{B_0}$ of *Equations (10)* and *(11)* from the measured $\Delta \boldsymbol{p_i^2}$ pressure differences belonging to $\boldsymbol{q_{gi}}$ gas flow volume rates.

The test requires 30 mm high test samples with a diameter of 37 mm. The height of the test sample closely resembles the thickness of the refractory concrete layer generally used for sealing the solidification hole of the refractory blocks in industrial practice.

2.2. Summary of gas permeability test results

Based on gas permeability tests performed on refractory concrete test samples made of Almatis CA-25 R cement and AZS powder, the following conclusions can be drawn (see Figure 3):

- The concrete used to seal the cavity of the refractory block is not gas resistant. The increase in the gas permeability of the concrete is linearly correlated with the pressure difference registered between the two ends of the tested sample.
- Layers below the outer surface (facing the combustion chamber) of the concrete sealing of the shrinkage cavity shows significantly lower flow resistance against steam formation. This means that the steam formed during the heating process in the outer layers of the refractory concrete can escape at much lower pressure differences with higher volumetric flux.

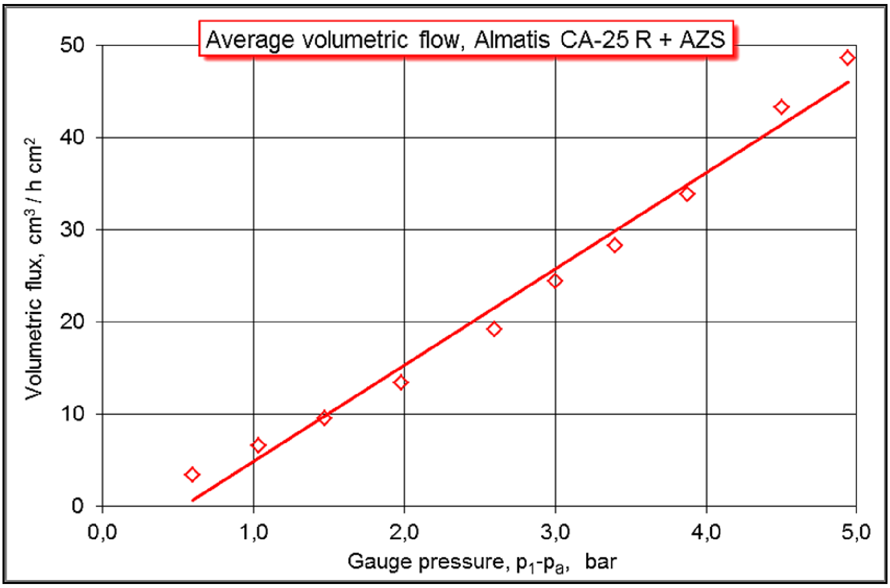

Figure 3. Average volumetric flow of concrete made from cement Almatis CA-25 R + grained AZS

3. Determination of temperature and overpressure in the solidification hole

3.1. Laboratory method for measuring temperature and overpressure in the solidification hole with measurement data

Test samples were made of refractory AZS blocks, with the dimension of 170 x 250 x 120 mm. In order to simulate the conditions of hole formation in electrofused refractory blocks, 80 mm deep and 60 mm wide cylindrical cavities were made, sealed with a 30 mm thick layer of concrete. The samples were placed in an electric furnace and heated to 350 °C at the rate of 5 °C/h.

A piezo-resistance differential pressure sensor, type "NSCDANN 150 PGUNV" [7] was connected to the outer end of the copper tube with a thick, transparent plastic tube charged with silicone oil (heat-resistant up to 300 °C) to prevent the steam from condensation and excess overpressure. The externally visible outer surface of this thermo-oil served as a visual indicator of the rising steam pressure in the closed hole.

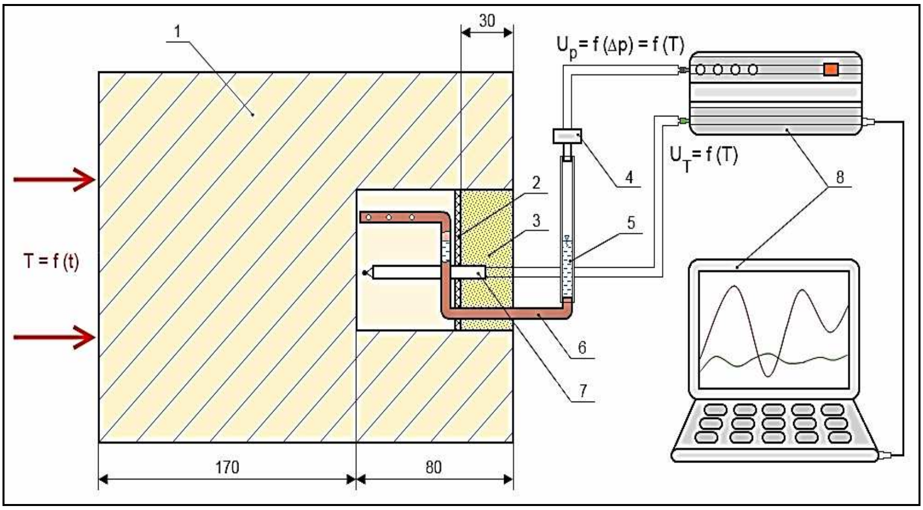

Figure 4. Schematic diagram of the measurement cycle for the monitoring of overpressure and temperature in the shrinkage cavity during the heat-up of an electrofused AZS (with a concrete-sealed solidification hole). 1 – refractory block, 2 – positioning copper mesh, 3 – tested refractory concrete, 4 – pressure sensor, 5 – heat-resistant silicone oil, 6 – copper tube, 7 – NiCr-Ni thermocouple, 8 – data collector

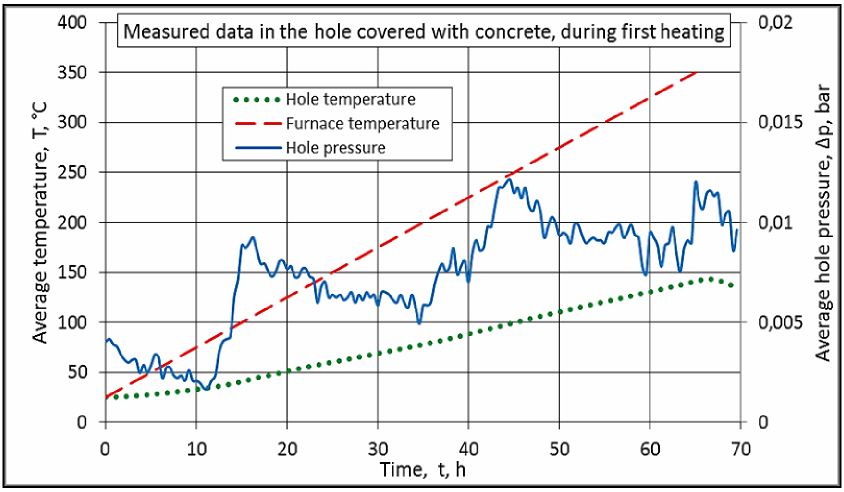

Figure 5. Average temperature and overpressure in the solidification hole, sealed with refractory concrete

3.2. Conclusions of the laboratory experiments

The following can be concluded from the laboratory measurement data:

- When the temperature inside the furnace and measured at the interior surface of the refractory is 250–260 °C, the solidification hole has a temperature of approximately 100 °C.
- Around 100 °C (i.e. the boiling point of water), the overpressure of the steam reaches its peak (max. 0,013 bar) for each tested sample. This means, that the gas permeability of the concrete allows the steam – formed from mechanical water – to release from the solidification hole at low pressure levels.

Final conclusions of the research

Based on the described complex analysis, it can be stated without a doubt, that the gas permeability characteristics of the refractory concrete made of cement Almatis CA-25 R + grained AZS, allows the steam, formed during the first heating up of refractory wall of glass melting furnaces, leave the block without further intervention.

The 0,02 bar overpressure – arising in the solidification hole – does not cause damage to the electrofused refractory blocks and the refractory concrete used for the lining of the solidification hole.

Acknowledment

This research was (partially) carried out in the framework of the Centre of Excellence of Sustainable Resource management at the University of Miskolc.

References

[1] MOTIM Fused Cast Refractories Ltd.: http://www.motim.hu/kadko/docs/felhasznalas.htm
[2] MOTIM Fused Cast Refractories Ltd.: Catalog of Fused Cast Refractory Blocks, 2012.
[3] MOTIM Fused Cast Refractories Ltd.: http://www.motim.hu/hu/fcr/csucstechnologia-es-minoseg
[4] ALMATIS: GP-RCP/005/R07/0211/MSDS 993; FGP-RCP_005_Calcium-Aluminate-Cement_0211.pdf
[5] Journal of Thermal Analysis, Vol. 32, pp. 301–309.
[6] Petzold,A.–Ulbricht, J.: *Feuerbeton*. Deutscher Verlag für Grundstoffindustrie, Leipzig, 1994.
[7] http://www.farnell.com/datasheets/1499905.pdf (2013. 09. 18.)

Materials Science and Engineering, Volume 39, No. 1 (2014), pp. 69–79.

THE EFFECT OF STRONTIUM AND ANTIMONY ON THE MECHANICAL PROPERTIES OF Al-Si ALLOYS

MÓNIKA TOKÁR[1]–GYÖRGY FEGYVERNEKI[2]–
VALÉRIA MERTINGER[3]

In the dynamically developing casting production sector, casting products designed for vehicles must satisfy more and more criteria to meet the increasingly stringent performance requirements. Nowadays, secondary alloys are frequently used in casting production, but the effects of impurity elements on secondary alloys are not yet well-known. It essential to recognize that the quantity of impurity elements in Al-Si alloys is related to the quality of the materials. Two elements are frequently used to modify the eutectic silicon phase of these alloys, namely strontium and antimony. After scrap recycling, these elements are included in the melt, where the strontium and antimony together may lead to the formation of intermetallic compounds. The aim of our research was the examination of the joint effects of antimony and strontium on the mechanical properties of aluminium-silicon alloys with different cooling rates.

Keywords: aluminium alloys, silicon modification, wall-thicknesses, mechanical properties.

Introduction

In the casting industry the term “modification” describes the method in which inoculants, in the form of master alloys, are added to the aluminium melt in order to promote the formation of a fine and fibrous eutectic silicon structure during the solidification process [1]. Eutectic modification is a common process employed for Al-Si base alloys to improve the mechanical properties, particularly the tensile elongation of the material, by promoting the structural refinement of the inherently brittle eutectic silicon phase. It is well-known that trace additions of strontium to hypoeutectic aluminium–silicon alloys result in a transformation – from a coarse plate-like structure to a well-refined fibrous structure – of the eutectic silicon morphology [2]. Impurities might weaken this modification effect thus, lead to the deterioration of the mechanical properties of the final product.

During our work, we casted a series of samples from a melt containing different concentrations of antimony and strontium. The planned concentration ranges were between 0-300 ppm of strontium and 0–340 ppm of antimony. We designed and then tested a casting geometry with various wall-thickness values (6 mm, 8 mm, 12 mm, 25 mm). Samples for the tensile test were produced from the casted products.

---

[1] University of Miskolc, Metallurgical and Foundry Engineering Institute
3515 Miskolc-Egyetemváros, Hungary
monika.tokar@uni-miskolc.hu
[2] University of Miskolc, Metallurgical and Foundry Engineering Institute
3515 Miskolc-Egyetemváros, Hungary
[3] University of Miskolc, Physical Metallurgy, Metalforming and Nanotechnology Institute
3515 Miskolc-Egyetemváros, Hungary
femvali@uni-miskolc.hu

Cooling curves were obtained and analysed, and quantitative metallography was used to determine the level of eutectic modification. We used an Instron 5982 type electromechanical tensile test machine with a tensile speed of 0.004 mm/mm/s to determine the mechanical properties of the tested samples; and a Zeiss EVOMA 10 scanning electron microscope (SEM) equipped with an EDAX system to investigate the fractured surfaces.

1. Experiment

In order to allow a comparative analysis of the experimental results obtained from the measurements with the respective parameters of industrial castings, a special casting geometry was designed with different wall-thicknesses representing different cooling rates. Figure 1. shows the schematic illustration of the casting die with 4 different wall-thicknesses and the positions of the tensile test specimens. “Solid Edge” software was used to design the multiple casting geometry. The best solution was selected by using “NovaFlow and Solid“ simulation. After the simulation process, the casting die with the optimised parameters was produced.

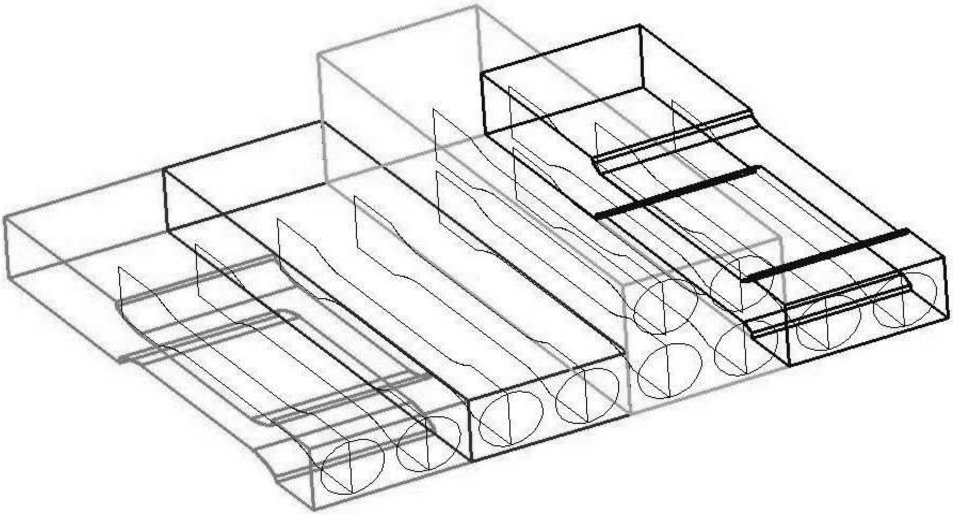

Figure 1. Schematic illustration of the casting geometry, with tensile rods

For experimental casting, we used standard AlSi8Cu3 (226.10) alloy ingots, their chemical compositions are given in Table 1. We used AlSr10 (Al-10wt.%Sr, wire) and AlSb10 (Al-10wt.%Sb, ingots) master alloys.

Table 1

Chemical composition of the AlSi8Cu3 *ingots*

Elements	**Si**	**Cu**	**Mg**	**Ti**	**Sr**	**Sb**	**Fe**	**Mn**	**Pb**	**Sn**
wt.%	8.85	2.53	0.30	0.10	0.0005	0.0040	0.51	0.35	0.05	0.01

A total amount of 100 kg of the AlSi8Cu3 alloy ingots were melted and 16 different alloys were casted in 4 experimental series. The strontium and antimony alloying matrix of the 4 experimental series can be seen in Table 2. After the melting process, antimony was added to the melt in the first step, and different strontium concentrations were applied before each casting process. After the addition of both modifier elements (Sb, Sr), the molten alloy was kept at constant temperature for 15 minutes.

Table 2

Strontium and antimony concentrations in the experimental matrix

Casting series	**Strontium (ppm)**	**Antimony (ppm)**			
1.	5 (base alloy)	40	140	240	340
2.	100				
3.	200				
4.	300				

Unvarying experimental parameters can be seen in Table 3.

Table 3

Unvarying experimental parameters

Melting and alloying temperature	775±5 °C
Casting temperature	765±5 °C
Preheating temperature applied to the casting die	400 °C
Stabilization time after alloying	15 min

2. Results

2.1. Modification level of the eutectic structure

The modification level was determined from the cooling curves with the follow the equation [1]:

$$\Delta T^{Al\text{-}Si}_{E,G} = T^{Al\text{-}Si}_{E,G,UNMODIFIED} - T^{Al\text{-}Si}_{E,G,MODIFIED} \qquad (1)$$

Figure 2 shows the calculated values as a function of real strontium and antimony concentrations.

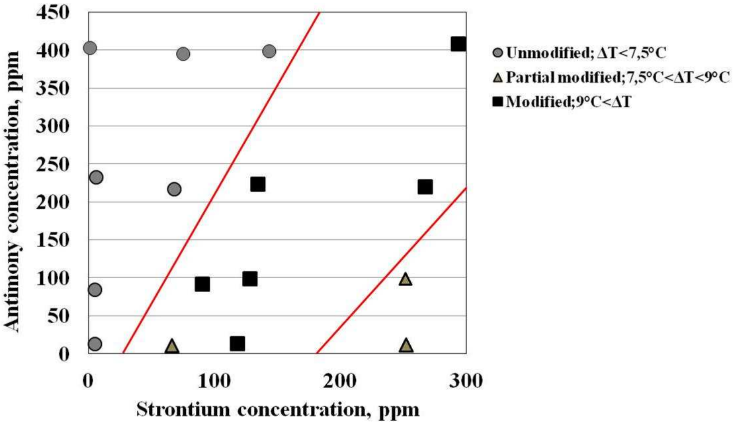

Figure 2. Eutectic modification levels calculated from thermal analysis cooling curves for real strontium and antimony concentrations (sampled after alloying followed by 15 min. stabilization time)

Based on the value of ΔT, two modification categories are mentioned in the published literature. If the temperature difference is less than 9 °C, the eutectic structure is signified as “non-modified”; if ΔT is higher than 9 °C, the structure is called “modified”. Observing the ΔT values on the cooling curve and the system of the tissues, we felt necessary to introduce a new grade. Thus, if the value is higher than 7.5 °C, but lower than 9 °C, the structure is referred to as “partially modified”.

The level of structural modification was also ranked based on the comparative analysis of the casted microstructure with standardized charts of similarly casted microstructures published by the American Foundry Society [3]. The results can be seen in Figure 3.

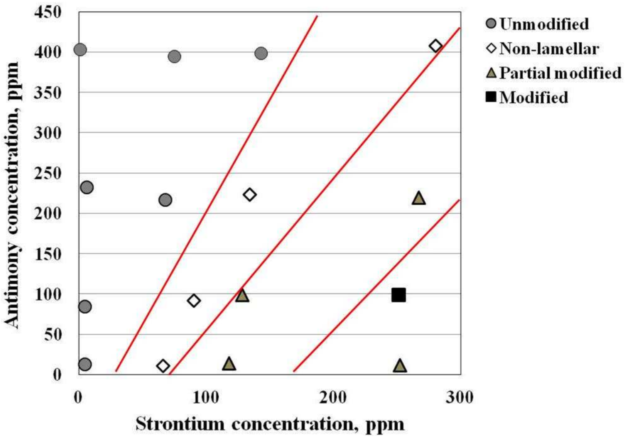

Figure 3. Modification levels determined by standard charts for real strontium and antimony concentrations (sampled after alloying followed by 15 min. stabilization time)

Based on the results of data analysis, the following can be summarized:

- If Sb concentration is increased, Sr concentration should be likewise increased so as to keep the same modification level.
- It can be observed, that the modification level of the samples with the highest Sb content from a given series with pre-determined Sr content is the same as the modification level of the samples with lower Sb content from another series with lower Sr content.

2.2. Mechanical properties

To determine the mechanical properties of the respective alloys, tensile rods from pre-selected sites were processed, as seen in Figure 4.

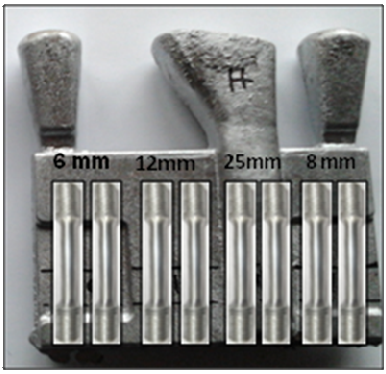

Figure 4. Casting, with tensile rods included

In Figures 5–8, tensile test results as a function of wall-thickness can be seen for alloys containing 5 ppm, 100 ppm, 200 ppm and 300 ppm of strontium, respectively. Generally, tensile strength values are decreasing with increasing wall-thickness, with an apparent maximum point at 8 mm wall-thickness.

In Figures 9–12, average tensile strength results as a function of Sr-Sb concentrations for different wall-thicknesses are represented. For 6 mm, 8 mm and 12 mm wall-thicknesses, a maximum distribution of the results can be seen, relative to the strontium concentrations. Depending on the antimony concentration, a maximum distribution of the results can be observed for some cases, however, this tendency cannot be generalized. In the case of 25 mm wall-thickness, it can be deduced from the results (obtained for Rm then for $Rp_{0,2}$, A) that other effects like porous structure formation could have more strongly influenced the results than the addition of various strontium antimony concentrations.

It can be observed from the diagrams, that ultimate tensile strength tends to reach its maximum when plotted as a function of strontium concentration at the given antimony concentration (Figures 13–15.).

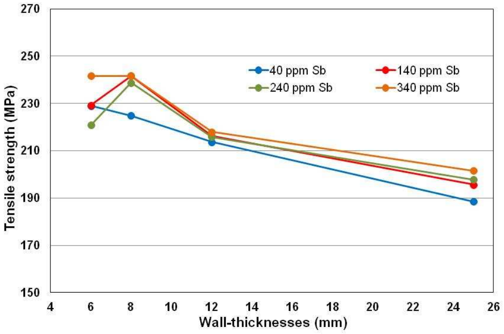

Figure 5. Average tensile strength values as a function of wall-thickness for 5 ppm of Sr

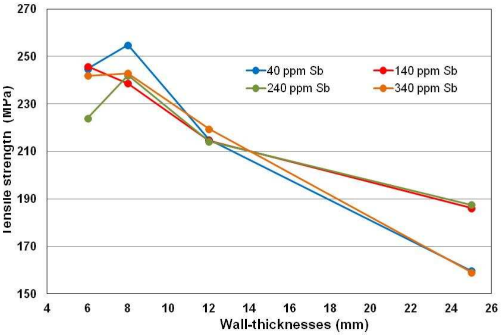

Figure 6. Average tensile strength values as a function of wall-thickness for 100 ppm of Sr

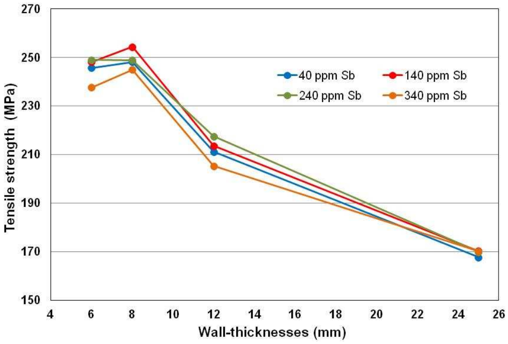

Figure 7. Average tensile strength values as a function of wall-thickness for 200 ppm of Sr

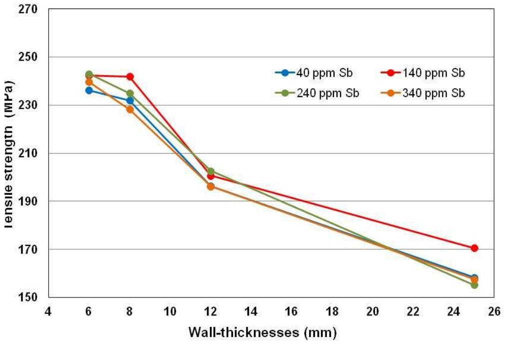

Figure 8. Average tensile strength values as a function of wall-thickness for 300 ppm of Sr

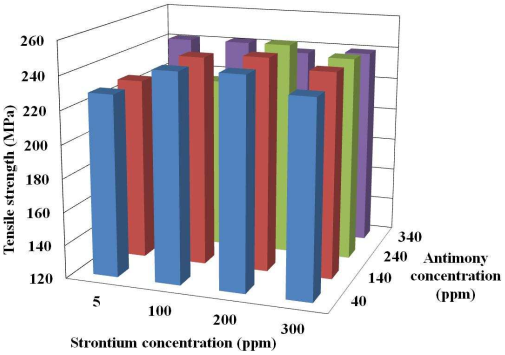

Figure 9. Average tensile strength values as a function of Sr-Sb concentrations at 6 mm wall-thickness

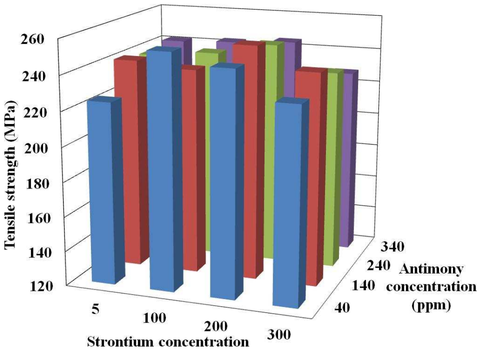

Figure 10. Average tensile strength values as a function of Sr-Sb concentrations at 8 mm wall-thickness

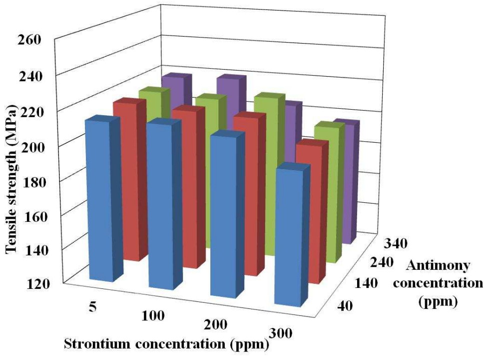

Figure 11. Average tensile strength values as a function of Sr-Sb concentrations at 12 mm wall-thickness

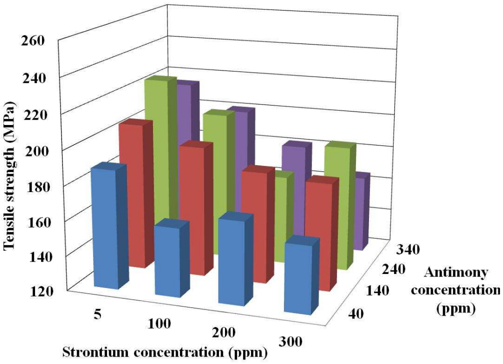

Figure 12. Average tensile strength values as a function of Sr-Sb concentrations at 25 mm wall-thickness

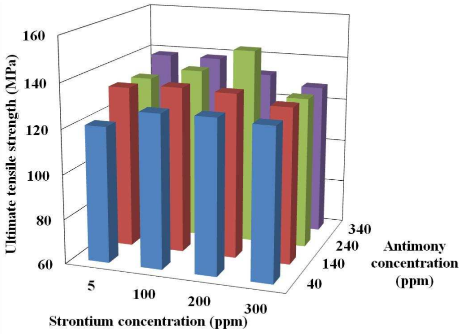

Figure 13. Average ultimate tensile strength values as a function of Sr-Sb concentrations at 6 mm wall-thickness

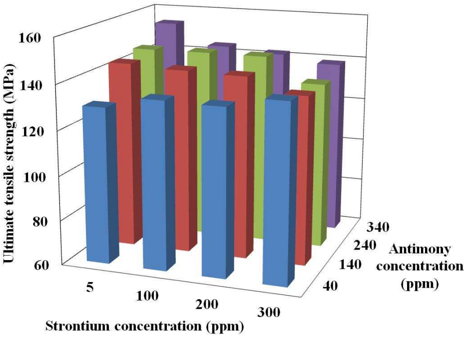

Figure 14. Average ultimate tensile strength values as a function of Sr-Sb concentrations at 8 mm wall-thickness

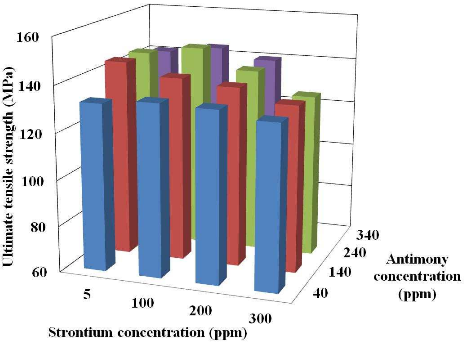

Figure 15. Average ultimate tensile strength values as a function of Sr-Sb concentrations at 12 mm wall-thickness

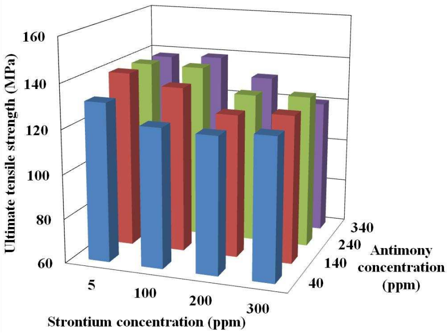

Figure 16. Average ultimate tensile strength values as a function of Sr-Sb concentrations at 25 mm wall-thickness

The tensile test results for elongation can be seen in Figures 17–20. as a function of strontium–antimony concentrations. With wall-thickness values of 6 mm, 8 mm and 12 mm, it can be observed that by increasing the strontium concentration – relative to the concentration of antimony – the elongation tends toward a maximum.

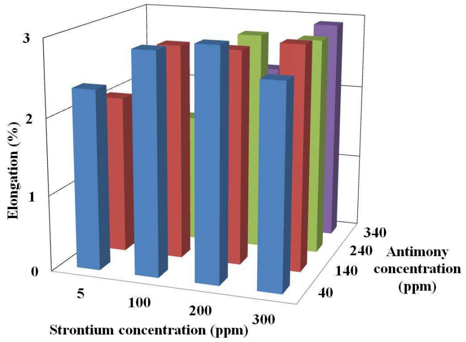

Figure 17. Average elongation values as a function of Sr-Sb concentrations at 6 mm wall-thickness

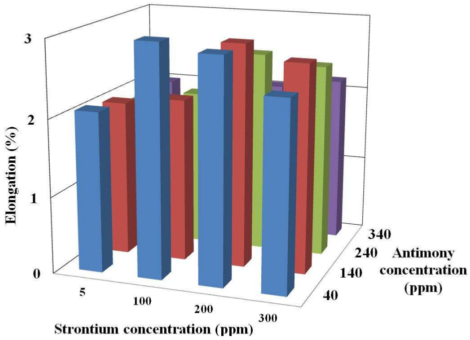

Figure 18. Average elongation values as a function of Sr-Sb concentrations at 8 mm wall-thickness

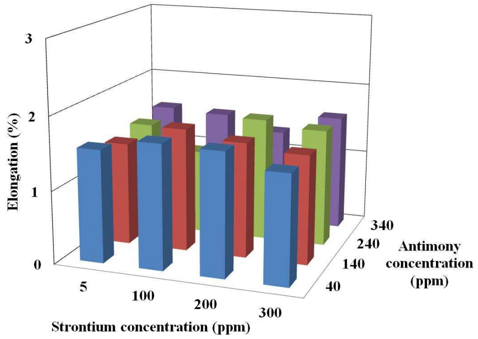

Figure 19. Average elongation values as a function of Sr-Sb concentrations at 12 mm wall-thickness

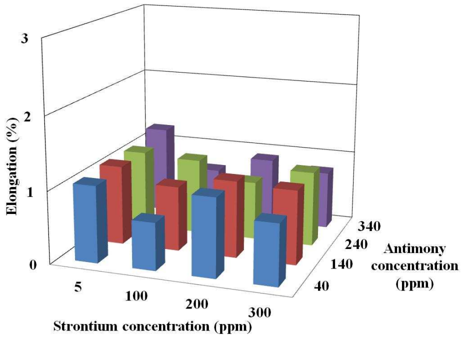

Figure 20. Average elongation values as a function of Sr-Sb concentrations at 25 mm wall-thickness

2.3. Fracture features

Based on the results, we have chosen two types of samples for SEM analysis. The first sample type, taken from a section with 25 mm wall-thickness, exhibited the most unfavourable mechanical properties. The second type, sampled form the section with 8 mm wall-thickness, seemed to have the most favourable mechanical properties. The samples presented below contained 300 ppm of strontium and 340 ppm of antimony.

It is apparent from the image processed on the fracture surface of the sample with 25 mm wall-thickness (with unfavourable mechanical properties), that different phases were formed in the Al-matrix [Figures 21 a–b)]. The EDAX results of the marked phases in Figure 21 b) is shown in Table 4. The phase marked No. 1 represents a strontium–antimony intermetallic compound, phase No. 2 is a Cu-rich phase, while phase No. 3 is a Pb particle. Figure 21 a) shows the fracture surface, characterized by a relatively high porosity volume fraction.

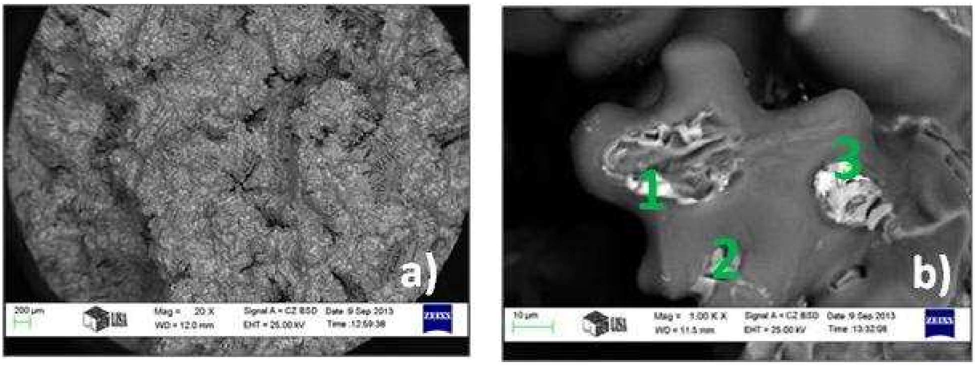

Figure 21 a–b) SEM fracture surface image for a rod section with 25 mm wall-thickness and unfavourable mechanical properties

Table 4

Results of the EDS analysis (25 mm)

Elements (wt.%)	No. 1	No. 2	No. 3
Si	5.61	2.52	2.93
Cu	5.11	**26.13**	2.33
Mg	5.82	1.14	0.64
O	**15.97**	–	–
Sr	**17.38**	–	–
Sb	**19.43**	–	–
Pb	2.42	–	54.89

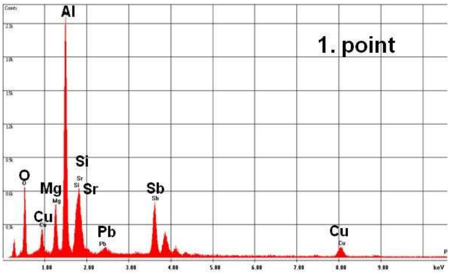

Figure 22. EDS analysis for Point 1

In Figures 23 a–b) we examined a sample section with 8 mm wall-thickness and with metallic contents of 340 ppm of Sb and 300 ppm of Sr. Comparing the images in Figures 21 a) and 23 a) it is clearly seen that both porosity volume fraction and the volume fractions of Sr-Sb compounds are considerably lower for the samples taken from the section with 8 mm thickness.

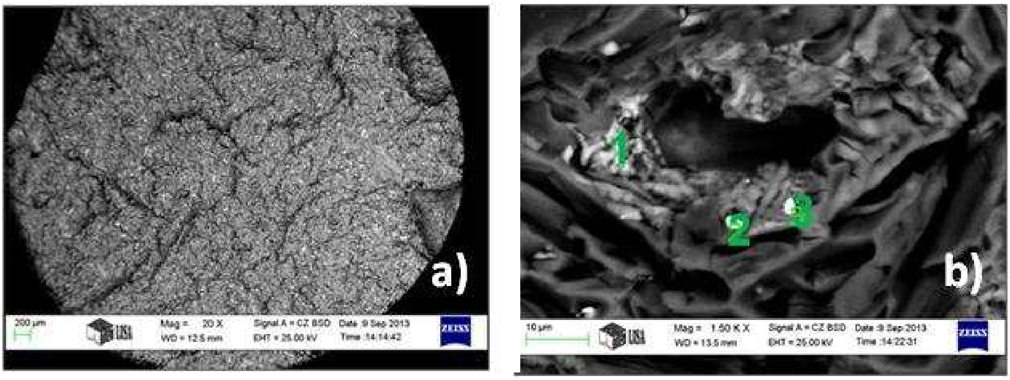

Figure 23.a-b. SEM fracture surface image for a rod section with 8 mm wall-thickness and favourable mechanical properties

Table 5

Results of the EDS analysis (8 mm)

Elements (wt.%)	**No. 1**	**No. 2**	**No. 3**
Si	7.52	12.21	4.42
Cu	**27.82**	2.18	4.25
Mg	5.82	1.38	0.53
Mn	–	–	0.68
Fe		–	1.48
Sr	–	**1.23**	1.37
Sb	–	**0.54**	–
Pb	–	38.11	–
Sn	–	2.65	–

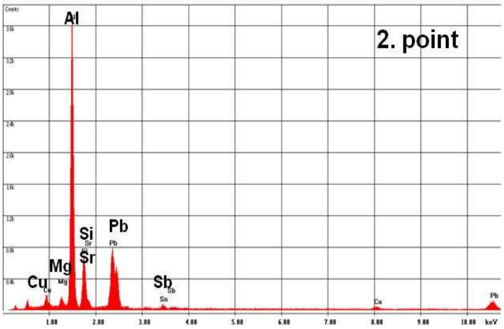

Figure 24. EDS analysis for Point 2

Conclusions

In this work, we studied the effect of different concentrations of antimony and strontium on the mechanical behaviour and the level of structural modification of Al-Si alloys, and the tendency of these alloys towards intermetallic compound formation. The concentration of antimony ranged from 40 to 340 ppm, while that of strontium varied between 5 and 300 ppm.

In this work, we presented the results of a comparative analysis of the eutectic modification levels determined with two different methods, namely thermal analysis and AFS standard charts. By evaluating the results obtained from these two types of characterization, it can be stated:

- If Sb concentration is increased, Sr concentration should be likewise increased so as to keep the same modification level.

- It can be observed, that the modification level of the samples with the highest Sb content from a given series with pre-determined Sr content is the same as the modification level of the samples with lower Sb content from another series with lower Sr content.

On the basis of the results obtained from the cooling curves, the term “partially modified level” was introduced, pertaining to a ΔT value lower than 9 °C, but higher than 7.5 °C.

Measuring the tensile strength and ultimate tensile strength values for 6 mm, 8 mm and 12 mm wall-thicknesses, we have demonstrated that the results – relative to the strontium concentration – follow a maximum distribution pattern. Relative to the antimony concentration, the same values show a maximum distribution for some cases only, thus, it cannot be called a general tendency. Considering the tensile test results for elongation at wall-thickness values of 6 mm, 8 mm and 12 mm, it can be observed that with an increase in the strontium concentration – relative to the concentration of antimony – elongation tends to reach a maximum. During the fracture analysis, we found some compounds that contained Sr and Sb together. The aim of our long-term research work is to study the effects of Sr-Sb intermetallic compound formation on Al-Si foundry alloys.

Acknowledgement

This research was realized in the frames of TÁMOP 4.2.4. A/2-11-1-2012-0001 “National Excellence Program – Elaborating and operating an inland student and researcher personal support system convergence program”. The project was subsidized by the European Union and co-financed by the European Social Fund.

References

[1] Djurdjevic, M.–Jiang, H.–Sokolowski, J.: *On-line prediction of aluminium-silicon eutectic modification level using thermal analysis.* Materials Characterization – Elsevier, 46 (2001), pp. 31–38.

[2] Dahle, A. K.–Nogita, K.–McDonald, S. D.–Dinnis, C.–Luc, L.: *Eutectic modification and microstructure development in Al-Si alloys.* Materials Science and Engineering, *A 413–414* (2005), pp. 243–248.

[3] Kaufman, J. G.–Rooy, E. L.: *Aluminium alloy castings properties, processes and applications.* ASM International (2005).

[4] Fatahalla, N.–Hazif, M.–Abdulkhalek, M.: *Effect of microstructure on the mechanical properties and fracture of commercial hypoeutectis Al-Si alloy modified with Na, Sb and Sr.* Journal of Materials Science, 34 (1999), pp. 3555–3564.

University of Miskolc, Department of Research Management and International Relations
Responsible of publication: Prof. Dr. Tamás Kékesi
Miskolc-Egyetemváros
Published by the Miskolc University Press under ledership of Erzsébet Burmeister
Number of copies printed: 161
Put to Press on 2014
Number of permission: TNO – 2014 – 60 – ME HU ISSN 2063-6792